

# Numerical modelling of the Sydney Basin using temperature dependent thermal conductivity measurements

Thesis submitted on the 9<sup>th</sup> of October 2015, by

Alexandre Lemenager

Department of Earth and Planetary Sciences,

**Macquarie University**



**MACQUARIE**  
University



# Table of contents

## 1. Introduction

1.1 Relevance and objectives	2
1.2 Study aims	3

## 2. Geological background

2.1 Basin framework	5
2.2 Heat flow	7
2.3 Thermal conductivity measurements	8
2.4 Thermal modelling	9

## 3. Methods

3.1 Thermal conductivity measurements	10
3.2 Finite element thermal modelling	16
3.2.1 Thermal modelling	16
3.2.2 Computational grid	17
3.2.3 Monte Carlo method	19
3.3 Physical model setup	19
3.3.1 Boundary conditions	19
3.3.2 Interpolation method	19
3.3.3 Spatial information	20
3.3.4 Profile geometry	21

3.3.5 Heat production values	25
4. Results	
4.1 Thermal conductivity measurements	27
4.2. Non-temperature dependent thermal profiles	33
4.3 Temperature dependent thermal profiles	37
4.4 Geotherm sections	42
5. Discussion	
5.1 Importance of temperature dependent thermal conductivity	47
5.2 Importance of coal	49
5.3 Effect of basin and basement geometry on thermal model	51
5.4 Additional implications	
5.4.1 Effect of geothermal gradient on crustal structure, rigidity and viscosity	53
6 Conclusion	54
References	i
Appendix	
The thermal model code	vi

## Abstract

The thermal structure of continental crust is a critical factor for geothermal exploration, hydrocarbon maturation and crustal strength, and yet our understanding of it is limited by our incomplete knowledge of its geological structure and thermal properties. One of the most critical parameters in modelling upper crustal temperature is thermal conductivity, which itself exhibits strong temperature dependence. In this study, finite-element geothermal models of the Sydney Basin are generated through the use of deal.II finite element libraries. Basin geometry and structure is adapted from Danis, et al. (2011), which quantified the extent of Triassic sediment, Permian coal measures, Carboniferous volcanics and Basement thickness. We find that temperature-dependent thermal conductivity result in lower lateral variation in temperature, compared to constant thermal conductivity models. However, the average temperatures at depth are significantly higher when temperature-dependent thermal conductivity effects are included. A number of regions within the Sydney Basin demonstrate temperatures above 150°C at depths of less than 2000m in these models, for instance NW of Singleton exhibits a strong thermal anomaly, demonstrating the potential for geothermal prospectivity of the region from experimentally-constrained thermal parameters. Future work will address the repeatability and application of this type of thermal model in areas of varying geology and stratigraphy.


## Acknowledgments

I would like to sincerely thank my supervisors, Craig O'Neill and Siqi Zhang who have taught me a lot and guided me through the world of academic research. A lot is still to be learnt, but I very much appreciate their repeated guidance and help along the way. I thank my peers who are also submitting their theses for all the moral support they have provided in times of need. I thank my family and friends who showed interest in my project and offered assistance when nothing was asked of them. And last but not least I would like to thank my parents especially for keeping a roof under my head and always being there for me.

This thesis is dedicated to those people and I wish fortune to all of those who have partaken in this thrilling journey of academic research, through the Macquarie University Master of Research program. Lastly I would like to thank CCFS for research funding and for the incredible research this program has produced over the years since its inception.

## Statement of originality

The material of this thesis has not been accepted for the award under any other degree to a university or tertiary institution other than that of Macquarie University, Australia. To the best of my knowledge and control, this thesis contains no material previously written and published by another author, except where referenced otherwise.



Alexandre Lemenager

Author



# 1. Introduction

In this study, temperature dependent thermal conductivity measurements are implemented in thermal models to constrain the temperature distribution in the Sydney Basin at depth.

Variables used to set-up the model have been adapted from Danis et al. (2012), who has produced thermal models of the Sydney Basin, based on constant thermal conductivity values. These thermal models were constrained using equilibrated borehole temperature measurements from shallow groundwater in the Sydney Basin. However, large scale effects of temperature dependent thermal conductivity have yet to be implemented in current models regarding the Sydney Basin.

This study aims to assess how much of an effect variable thermal conductivity has on the large scale temperature distribution of the Sydney Basin, particularly when compared against constant thermal conductivity models.

To do this, finite element simulations were performed which result in a model of the temperature distributions of the Sydney Basin at depth, incorporating the effects of the basin stratigraphy, heat producing values and variations in thermal conductivity.

The thermal conductivity of Sydney Basin sediments (incorporating sandstone and coal) and basement (consisting of Lachlan Fold Belt granitoids) have a significant temperature dependence based on the measurements used in this study. It is currently thought that the addition of temperature dependent thermal conductivity data in geothermal simulations will result in significantly different temperature distributions at depth. For example, a drop in the thermal conductivity of sediments with increasing temperature, could result in greater simulated temperatures at depth, this constitutes critical information on the distribution of potential high temperature domains that may be prospective for geothermal energy.



## 1.1 Relevance and objectives

The need for better understanding of heat distribution at depth in the Sydney Basin was encouraged by previous models relying on non-equilibrated borehole temperature measurements conducted by Geoscience Australia (Gerner et al. 2010). It was found by Danis et al. (2012) that groundwater temperature re-equilibration can be a slow process, and has a far reaching impact on the true temperature of the surrounding aquifers directly post-drilling. Geoscience Australia's initial models showed large temperature anomalies with large differences (of  $>100^{\circ}\text{C}$ ) between each maximum and minimum temperature at 5km depth. On re-inspection of the original drilling reports, Danis et al. (2012) suggested that many of these discrepancies were due to non-equilibrated borehole measurements. As a result, there was a strong requirement for accurate temperature estimates of the Sydney Basin, in order to better assess and identify potential geothermal targets. Predictions and qualitative models heavily rely on the accuracy and precision of equilibrated borehole temperature measurements as well as the material constants used.

The geothermal potential of pre-extensional basins such as the Great Artesian Basin and extensional basins such as the Sydney Basin, have been relatively well studied. The recent study by Danis et al. (2011) has developed new methodologies to constrain the geothermal structure of the Sydney Basin, and its potential as an unconventional geothermal resource. The work discussed in this thesis largely builds on Danis et al. (2011) and (2012)'s work by incorporating temperature-dependent thermal conductivities based on laboratory measurements, rather than constant thermal conductivities previously used.

As a result, a compilation of datasets are used to construct and constrain the model design of the large scale finite element numerical models developed here through the integration of the deal.ii finite element libraries as the foundation of this model.

## 1.2 Study Aims

The aims of this project are listed as:

- To compile both existing datasets and new data, to construct a model of the temperature-dependent thermal conductivity of the Sydney Basin, including Lachlan Fold Belt granites (Evans 2013), the Sydney Basin Triassic sediments and Permian coal measures (used in this study).
- Incorporation of internal heating coefficients for both heat-generating sedimentary and volcanic units (Facer 1980) and basement rocks (Blevin 2010).
- To compile the raw gravity models of Danis et al. (2011) to constrain the geological structure of our deal.ii models, and facilitate the incorporation of this data into the deal.ii framework.
- Implementation of relevant deal.ii base code (Bangerth 2007) and methodologies such as 3<sup>rd</sup> order interpolation and Newton's method to solve non-linear, temperature-dependent thermal models.
- Implementation of Monte Carlo simulations in order to retrieve 1D geotherms and uncertainties from thermal models, with uncertain input parameters, and outline basin temperature distribution based on those geotherms.
- Compare temperature-dependent and constant thermal conductivity thermal models and address relevance of temperature dependent values on model.
- Interpret thermal models for their impact on the thermal structure of the Sydney Basin.

## 2. Geological background

The Sydney Basin can be described by a two-phase stratigraphic model for foreland basin development. The Sydney Basin formation process consisted of a foreland-basin deposition component - a result of tectonic loading (the syn-orogenic phase), and a basin response to thrust-belt erosion (post-orogenic phase) (Heller et al. 1988).

The Sydney Basin is located between the New England and Lachlan Fold belts, and consists of Permian-Triassic sedimentary sequence of at least 4km thick (Middleton et al. 1982). At its thickest point, the Sydney Basin is cross-cut by the north-easterly dipping frontal thrust fault of the Tamworth Arc of the New England Fold belt, and gradually thins towards the south (Conaghan et al. 1982). This trend is evident in the compiled gravity profiles sourced from Danis et al. (2011) used to define basin geometry at a relatively high spatial resolution. The Sydney Basin is essentially comprised of a succession of Permian to Triassic sedimentary and scattered volcanic rocks as a result of basin extension, outcropping in a NW to SE trend.

Fore-arc basin sedimentation and orogenic recession via crustal thinning has resulted in thermal subsidence, accumulating large coal reserves - among some of the largest in the world (Casareo 1996). These large coal reserves mostly consist of the Northern Sydney Basin Permian Coal Measures. Local bioturbations have been found to protrude the Newcastle coal measures, while the Newcastle coal measures have a predominantly dominant fluvial signature, containing plant fragments and upward fining sandstone and overbank sediments such as claystone (Hunt et al. 1984). The Newcastle coal measures appear as lenses within a large suite of terrigenous sediment (Herbert 1995). Therefore for the purposes of this work, the Newcastle and Tomago coal measures are grouped as one major coal layer with their terrigenous components reflected in their bulk thermal conductivity. Figure 1.2 shows the configuration of Newcastle and Tomago coal lenses.

The Tomago and Newcastle coal measures lay at the base of the Waratah Sandstone (Conaghan et al. 1987). Thick conglomerates of the upper Newcastle coal measures contain acid volcanic pebbles, with high pebble to sandstone ratios, hence preserving high portions of the primary protolith which represents a large bulk of the conglomeritic sequences (Hunt et al. 1984). The conglomerates likely originate from

braided alluvial fan deposits in the north east section of the basin. The likely source of sediment is the New England fold belt and Carboniferous mafic volcanics at the top of the basement, which was first identified from a positive gravity ridge between Bathurst and the Dural vicinity (Qureshi 1989). Sulphur content has been measured to be between 0.55 and 1%. Relative to the Sydney, Gunnedah and Bowen Basins this is characteristic of seams formed in deltaic (mainly lower delta plains) depositional environments (Hunt et al. 1984).

The Waratah sandstone sequence denotes a period of extended transgression and has signs of re-working indicating evidence of basin-wide shoreline re-working shown by angular unconformities at the contact between the Tomago and Newcastle coal measures (Conaghan et al. 1987). The Waratah sandstone marks a geological point separating organic rich coal sequences and largely terrigenous material, the Triassic sediments.

## **2.1 Basin framework**

The thermal structure of sedimentary basins is complex in nature. A basin's geometry, geology, and geophysical attributes affect its geodynamic behaviour and characteristics (Danis et al. 2012). Thus it is a fundamental requirement to understand a basin's geometry when dealing with unconventional geothermal modelling.

Finlayson et al. (1981) used seismic arrival times to constrain the crustal structure of the Sydney Basin, and suggested that the top of the basement in the Northern quadrant of the Sydney Basin was much closer to the surface than the Southern quadrant (Figure 1.1). Seismic surveys indicate that Singleton sediments have very low seismic velocities (around 5km/s) which may be up to 2km thick. Low seismic velocities are associated with the abundance of coal measures in the Singleton vicinity.

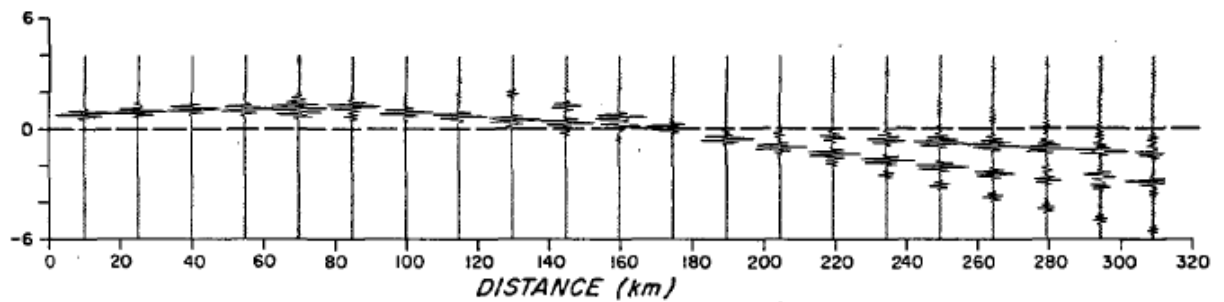


**Figure 2.1: Seismic record travel-time section between Singleton and Marulan**  
(extracted from Finlayson et al. 1981)

A seismic study by Greenhalgh et al. (1986) utilized a surface reflection profiling method to map the shallow coal seam structure of Hunter Valley coal seams. However they found in regions of thick Triassic sandstone cover, coal seams are undifferentiable. Another method is needed to effectively spatially define coal measures.

Early stage interpretations contributed by Finlayson et al. (1981) provide useful large scale spatial data, but the top 2km consisting of sediment is undifferentiated. Coal measures have a significant effect on basin heat distribution due to its naturally low thermal conductivity (Clauser et al. 1995; Danis et al. 2012). Understanding where coal is and how thick coal measures are is crucial to realistically depicting the crustal component of the Sydney Basin.

A paper released by Herbert (1995) provided high resolution sequence stratigraphy of the Sydney Basin (the top 1200m), identifying major coal seam (Figure 1.2). Coal measures are depicted as thin lenses alternating with other sediments. Although coal measures may be accurately displayed, a broader differentiation between coal-bearing sequences and other sediments, is needed for large-scale basin models.

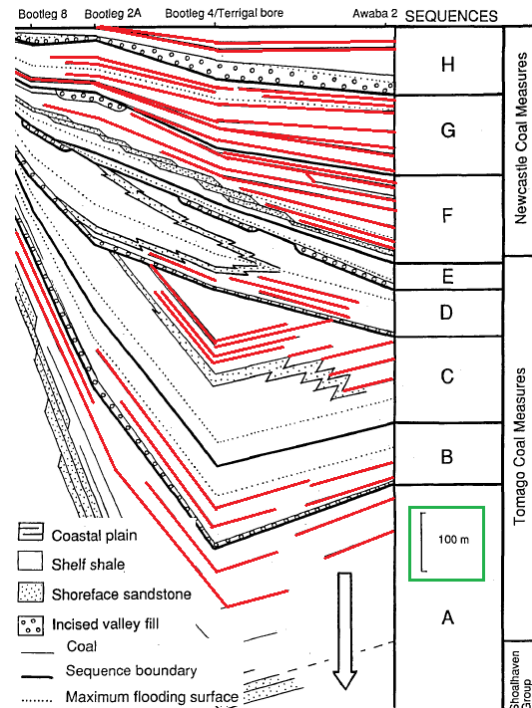


**Figure 2.2: Sequence stratigraphy linearly interpolated between West Newcastle and West Campbelltown. Green box shows scale, red lines show coal measures (extracted from Herbert, 1995)**

Large scale geological and structural interpretations are increasingly based on geophysical inversion methods (Quenette et al. 2012). Therefore, combining geophysical techniques and stratigraphic reconstructions would be, in that regard, highly effective. Danis et al. (2011) in essence combines large scale structures with fine enough resolution to construct a representative large scale geological model of the Sydney Basin through gravity and magnetic modelling methods.

## 2.2 Heat flow

Heat flow data can be used to infer independent heat production rate estimates of uranium and thorium in the continental crust (Jaupart et al. 2004). The energy that is produced from the radioactive decay of these elements accounts for a large proportion of the heat flow at the surface of continents (Jaupart et al. 2004).

The vertical scale of variation in heat production has been investigated through the KTB borehole in Germany, showing a variation in heat production between  $<0.5$  to  $\sim 3 \mu\text{Wm}^{-3}$  with no systematic trend with depth (Jaupart et al. 2004). Variation in heat production is hence highly dependent on the geology. Additional variables such as

groundwater circulation and large scale metamorphic alteration seem to have limited effects on the distribution of heat production with depth.

However, surface heat flow amplitude as a function of heat production variation can show trends that are characteristic at certain depths. Surface heat flow variation is much greater than heat flow variation at 10, 20 or 30km (Jaupart et al. 2004). Temperature variation at 10km depth or more would hence exhibit much less variation than near the surface. This is an important control in geothermal modelling when considering what the boundary conditions should be. Selecting a uniform bottom temperature at 12km ensures that the amplitude of heat flow variation is low enough to put a constraint on the bottom temperature boundary condition, which in this study is 350°C, as per Danis et al. (2012) thermal models.

### **2.3 Thermal conductivity measurements**

The Earth's interior heat is propagated by three main processes: radiation, advection and conduction (Clauser et al. 1995).

While radiation and advection play an important role in heat propagation, conduction is thought to be the dominant heat propagation mechanism in sedimentary basins, alongside advection of heat through groundwater motion (Clauser et al. 1995). Conduction itself is dependent on the composition of the medium (thermal conductivity), its temperature (in the case of temperature-dependent thermal conductivity), and the temperature gradient across a system.

A rock may be regarded as isotropic or anisotropic with regards to thermal conductivity. The thermal conductivity of volcanic and plutonic rocks is largely isotropic (Clauser et al. 1995). On the other hand, the thermal conductivity of sedimentary and metamorphic rocks is often anisotropic. Anisotropy found in sedimentary and metamorphic rocks is due to several factors including the microstructure of a rock - where its mineral assemblage may be intrinsically anisotropic, grain orientation and rock texture (Clauser et al. 1995). Sedimentary and metamorphic rocks may still be isotropic should anisotropic minerals be orientated randomly across a sample, or if a rock's texture, such as bedding, has little impact on the bulk thermal conductivity (Clauser et al. 1995).

The thermal conductivity of a specimen may be measured in situ or in the laboratory. In situ measurements accounts for a larger volume of rock, while it is easier to control temperature, pressure and pore-fluid variables with laboratory measurements (Clauser et al. 1995).

A rock's thermal conductivity isn't constant throughout. Statistical quantities such as histograms, median, mean and standard deviations are used to effectively understand a rock's thermal conductivity range and uncertainty (Clauser et al. 1995).

In addition to a rock's isotropy or anisotropy, thermal conductivity is a function of temperature (Clauser et al. 1995). Generally, thermal conductivity reduces with temperature, as differential expansion can lead to contact resistances between grains boundaries.

## **2.4 Thermal modelling**

Thermal modelling of the Sydney Basin has recently been undertaken by Danis et al. (2012), as part of the large-scale study of the wider Sydney-Bowen-Gunnedah Basin (Danis et al. 2010). Thermal models of Danis et al. (2012) were developed using a finite element code, named "Underworld" designed by Moresi et al. (2007). The model applies a constant top and bottom conditions of 15°C and 350°C respectively, with reflecting side conditions. The top temperature of 15°C was adopted from Cull's (1979) yearly average surface temperature measurements of the Gunnedah Basin. The bottom temperature of 350°C was constrained through extrapolation of groundwater borehole temperature measurements, taken across the Sydney Basin, and this boundary condition was modified to optimise the fit between the steady-state models, and observed geotherms.

Numerical models by Danis et al. (2012) incorporate the effects of basin architecture and geology with known temperature conditions in order to predict the thermal structure of the Sydney Basin. Additional emphasis was put on the refraction of heat around insulating coal layers and their seemingly decisive control on thermal profiles. As a result, the impact of coal in thermal models warrants further examination. The thermal models of Danis et al. (2012) also took into account the topography of the thermal profile, through ground surface elevation measurements. Topographic surface variations result in localised additions or deficiencies of sedimentary cover,



which can have a significant effect on subsurface temperatures, and shallow heat flow directions (Danis et al. 2012).

Figure 1.3 is a thermal model generated by Danis et al. (2012). Irregular basin geometry (basement refraction on the far west side of the model) and distance to top of basement result in isotherm retreat in some areas of low sedimentary cover. Inversely, the local isotherm in areas of thick sedimentary cover increases quite significantly. This model illustrates the 150°C isotherm beneath 4km of sedimentary cover with a high topography (circled in figure 2.3).

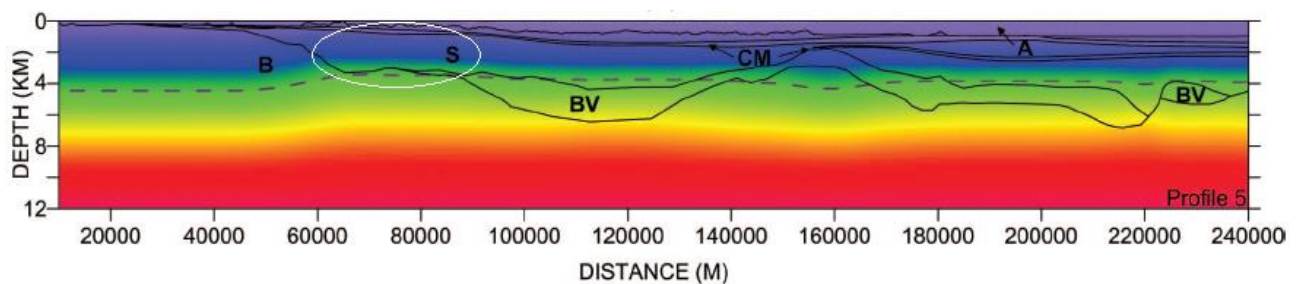


**Figure 2.3 Thermal model extracted from Danis et al. (2012)**

### 3. Methods

The ultimate aim of this thesis is to understand how temperature-dependent thermal conductivities, derived from new laboratory measurements, impact models of the thermal structure of the Sydney Basin. As such this work has two main prongs: i) to introduce new temperature-dependent conductivity measurements for the Sydney Basin, compile existing measurements, and collate related data, and ii) develop 2D deal.II finite element models for the thermal state of the Sydney Basin.

A number of datasets have had to be compiled in order to realistically characterise the model. The parameters which have been used to constrain the model include:

- Spatial information (large scale geology and elevation at a fine enough resolution)
- Equilibrated temperature extrapolations (extracted from borehole measurements at various depth)

- Temperature dependent thermal conductivity of the geology and internal precision / standard deviation of thermal conductivity measurements
- Heat production values (radiogenic heating)

### 3.1 Thermal conductivity measurements

Thermal conductivity values are based on measurements taken from a thermal conductivity tester, (Anter model 2022 – guarded heat flow apparatus) which are calibrated using standard calorimeters (stainless steel calorimeter: 19.05mm thick, small vespel calorimeter: 3.175mm thick, medium sized vespel calorimeter: 9.525mm thick). The Anter model 2022 has an effective accuracy range of 3 to 8% as described by The Anter Manual, accuracy is said to be largely affected by the thermal resistivity of the sample.

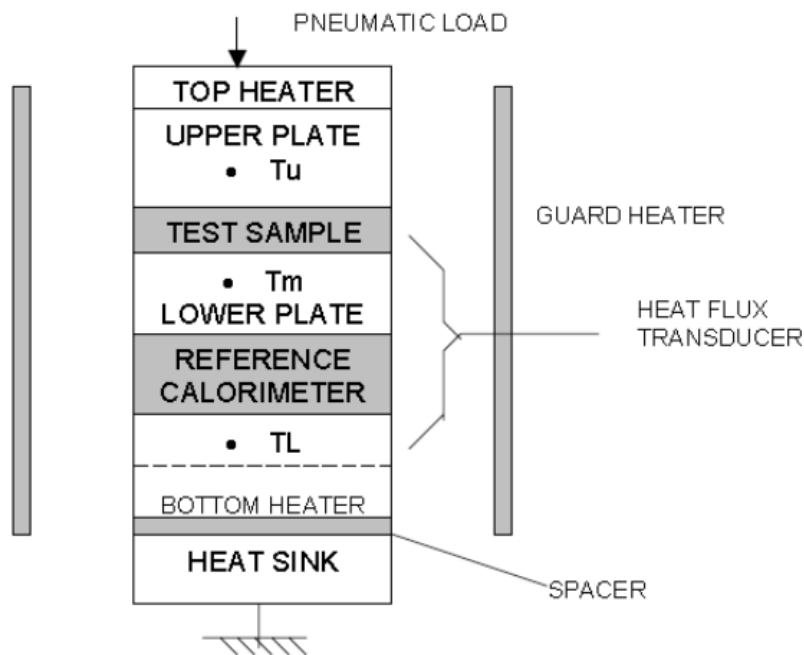


**Figure 3.1** *Sketch of the interior set up of the guarded heat flow apparatus (TA instruments & Anter Corporation 2011 Manual)*

At thermal equilibrium, the Fourier heat flow equation applied to the test stack becomes (Anter Manual 2011):

$$R_s = F * \left[ \frac{T_u - T_l}{Q} \right] - R_{int}$$

$R_s$  is thermal resistance of the sample,  $F$  is the heat flow transducer calibration factor,  $T_u$  is the upper plate surface temperature,  $T_l$  is the lower plate surface temperature,  $Q$  is the heat flow transducer output and  $R_{int}$  is the interface thermal resistance. The sample thermal conductivity  $\lambda$ , is calculated from (Anter Manual 2011) by dividing sample thickness by its measured thermal resistance from the previous equation.

$$\lambda = \frac{d}{R_s}$$

The pneumatic load is set at a constant 20MPa throughout thermal conductivity measurements.

#### *Internal precision values and calibration*

A set of calorimeters were used in the thermal conductivity measurement process, of sandstone, coal, and granite in the laboratory. The most recent calibration done on the samples measured is shown in the form of a calibration curve in figures 3.5 and 3.6.

Calibration specimens were repeatedly measured to constrain instrument internal precision values. Each calibration specimen was measured a total of three times, excluding the initial calibration process. These measurements were compared to initial calibration values, and their deviation from original measurements was recorded. Internal precision measurements were only done for low temperature set points, as the uncertainty in thermal conductivity is highest at low temperatures. The following plots show thermal conductivity variation of calibration specimens with repeated measurements.

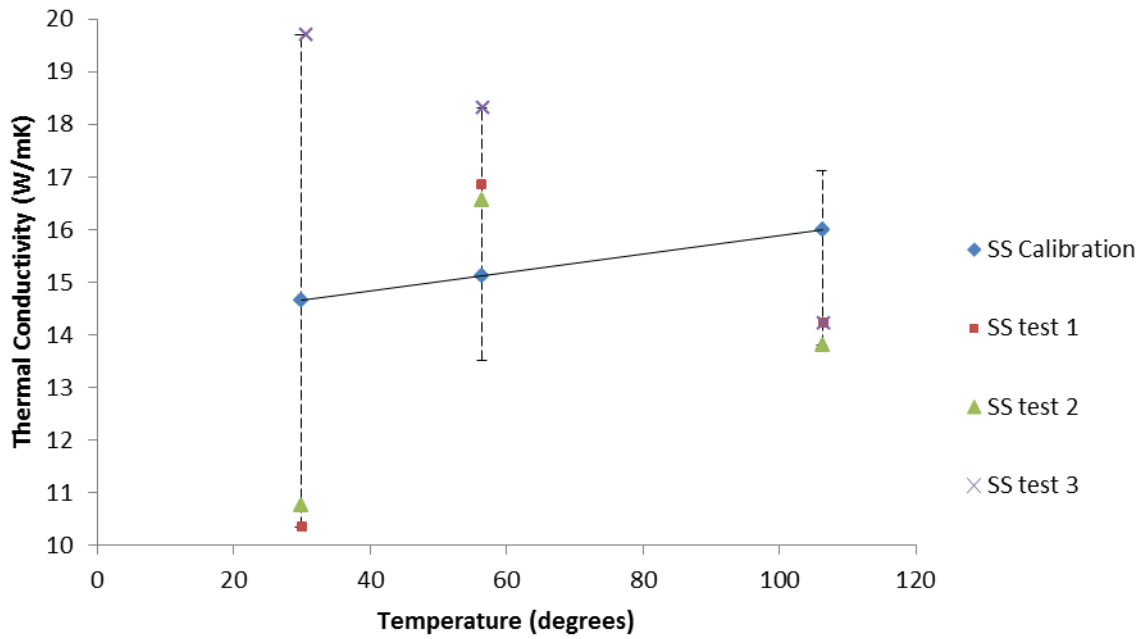


**Figure 3.2 Internal precision values for the stainless steel calorimeter (19.05mm), three sets of measurements were made relative to initial calibration measurements, error bars are not representative of true uncertainty, and instead capture the largest recorded uncertainty for each temperature set point**

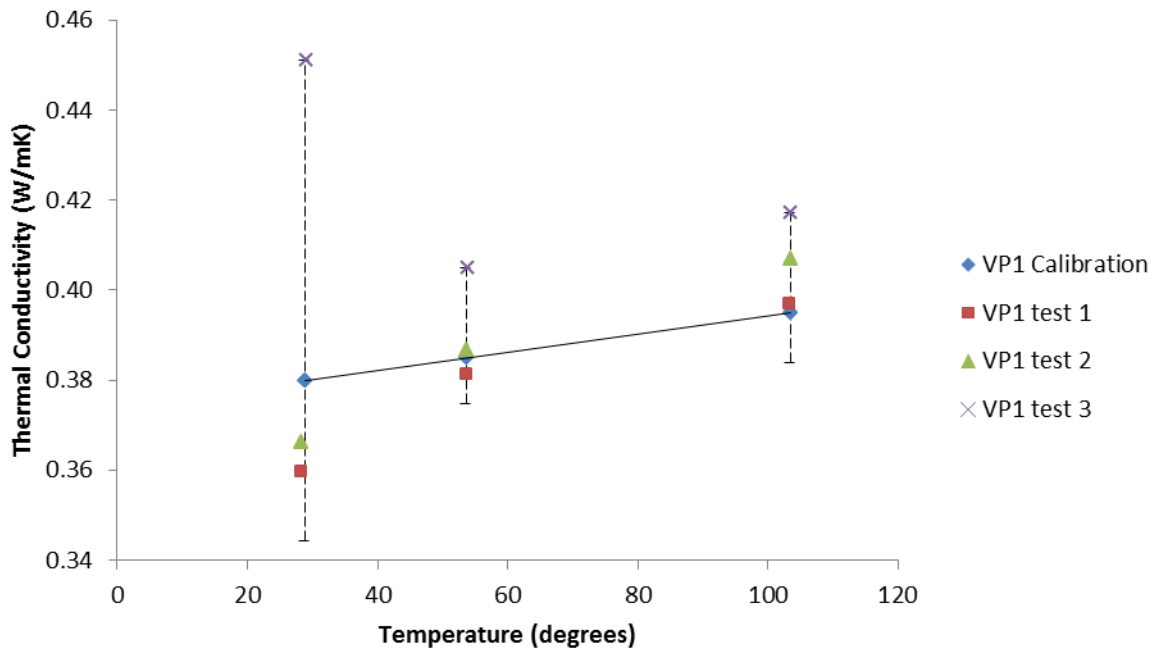


**Figure 3.3 Internal precision values for vespel 1 calorimeter (3.175mm), three sets of measurements were made relative to initial calibration measurements, error bars are not representative of true uncertainty, and instead capture the largest recorded uncertainty for each temperature set point**

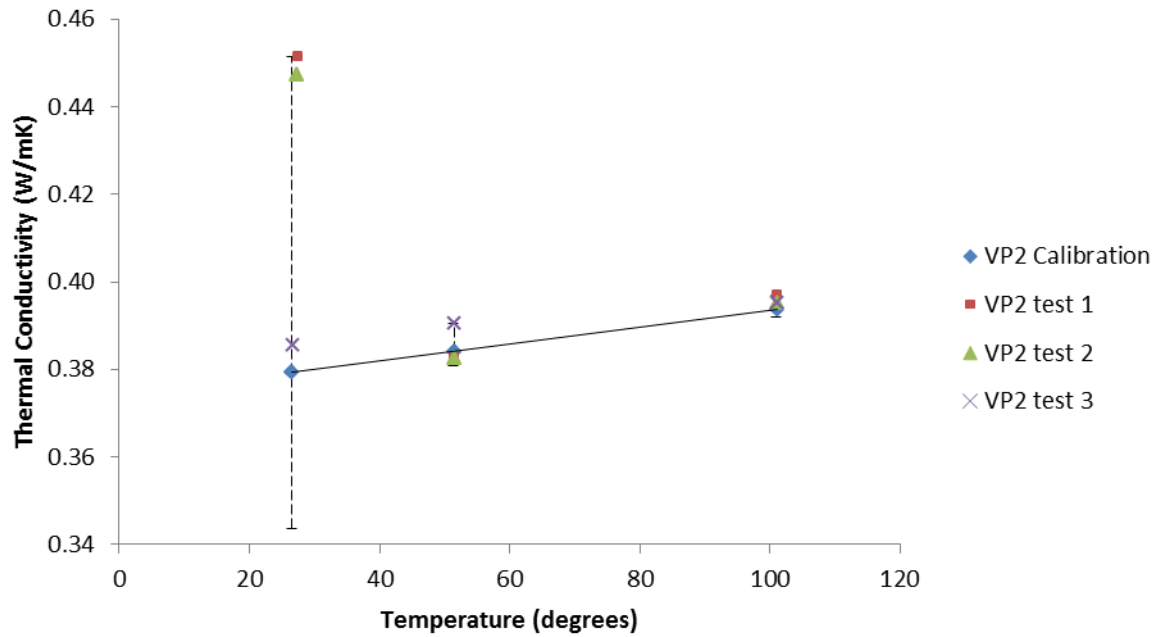


**Figure 3.4 Internal precision values for vespel 2 calorimeter (9.525mm), three sets of measurements were made relative to initial calibration measurements, error bars are not representative of true uncertainty, and instead capture the largest recorded uncertainty for each temperature set point**

As the internal precision measurement plots suggest, uncertainty between measurements reduces greatly with temperature. Therefore, internal precision for high temperature set points tests did not seem imperative, instead the uncertainty associated with the 100°C temperature set point can be used for high temperature measurements and still provide an uncertainty range for temperatures between 150 and 300°C.

Thermal conductivity tests of samples were done at pre-determined temperature intervals, of 20, 50 and 100 degrees for low temperature tests; and 100, 150, 200, 250 and 300 degrees for high temperature tests. Low and high temperature tests are performed separately, as they each require different spacers manufactured from copper and polyimide respectively. Each spacer is selected for its affinity to retain a relatively stable thermal conductivity within a low and high temperature range.

Minimum standard deviations were assigned to each specimen which were calculated based on the repeated thermal conductivity measurement of calibration specimens. Standard deviation values were derived from one calibration only, the

same calibration used for the coal thermal conductivity measurements. Low and high temperature calibration plots are shown below.

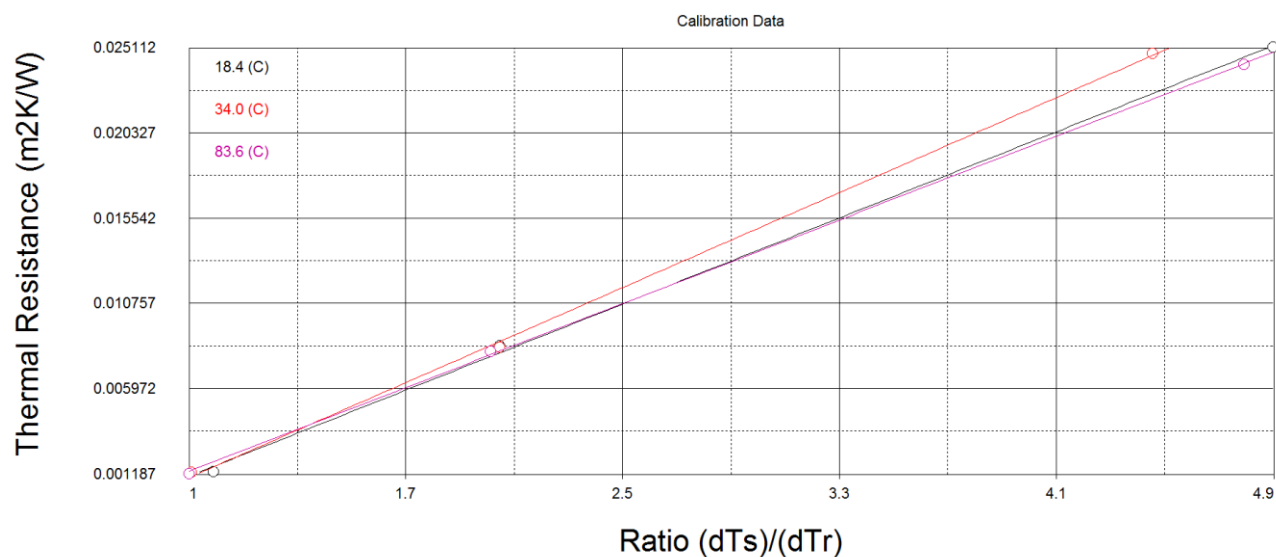


**Figure 3.5 Low temperature calibration plot for coal samples, thermal resistivity is plotted against the ratio between the difference in specimen temperature and reference temperature**

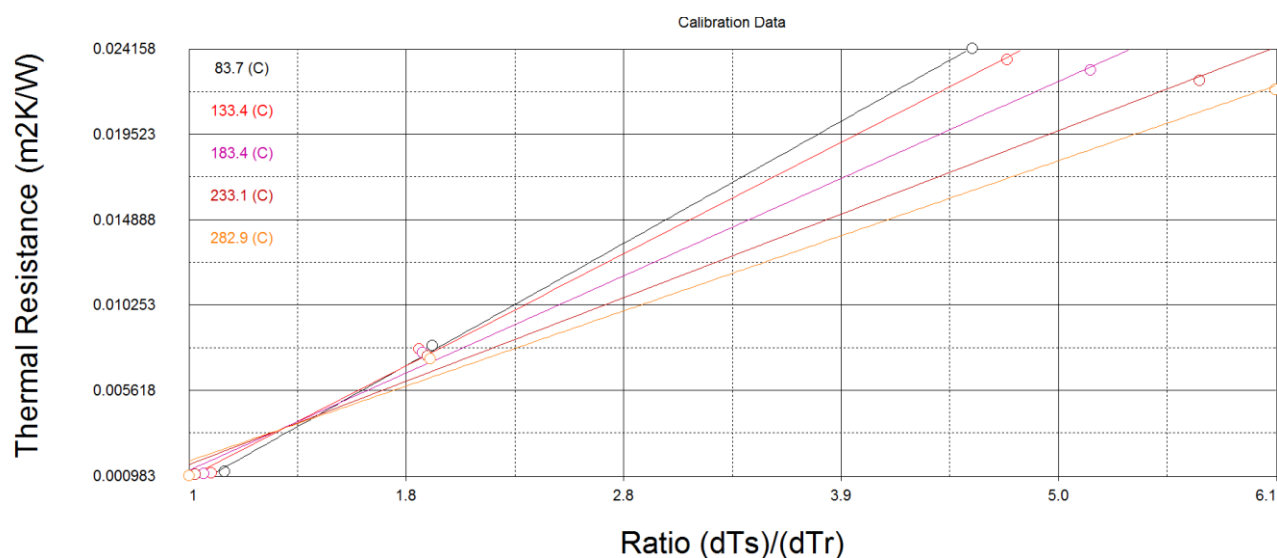


**Figure 3.6 High temperature calibration plot for coal samples, thermal resistivity is plotted against the ratio between the difference in specimen temperature and reference temperature**

Standard deviation values attributed to the thermal conductivity measurements of our samples were calculated by finding the standard deviation of internal precision values at each temperature set point. Internal precision measurements were made with three different calorimeters, which all have different thermal conductivities. Therefore,

an average of all standard deviation at each specific temperature was made. This standard deviation was then taken as a percentage of the initial calibration value. This percentage was then used to provide a standard deviation by percentage to the thermal conductivities of coal, sandstone and granite samples. Thermal conductivity measurements made on the sediment and granite samples however used different calibrations. For simplicity, internal precision values were taken from one instrument calibration, and its associated uncertainties were used for all samples, including the sandstone and granite samples.

As previously stated, respective standard deviations were applied by percentage of the original internal precision test. Thus, the higher the thermal conductivity, the higher the error is, based on this methodology. This observation is congruent with high uncertainties associated with the stainless steel calorimeter, which has a very high thermal conductivity. It was found that the lowest calibrated temperature set point (20 degrees) has by far the highest uncertainty. This is an instrumentation effect, caused by a counter balance of induced cooling and ambient heating required to attain thermal equilibration at low temperatures. As a rule, uncertainties gradually reduce with higher temperature set points (>50 degrees).

Thermal conductivity tests are designed in such a way that, low and high temperature thermal conductivity tests overlap at the 100 degree temperature mark. This effectively provides a basis for thermal conductivity variation at a single temperature set point without the requirement for internal precision tests. As a result, it was decided that the 100 degrees set point overlap was going to be used as the most reliable calculated standard deviation for all samples used as reference. It must be stated that the standard deviation used for the 20 degree set point, is directly calculated from the percentage standard deviation from the internal precision test. In order comply with the previous observation that the uncertainty associated with thermal conductivity measurements decrease with temperature, an average is made at the 50 degrees set point between the 20 degree and 100 degrees set points. This was opted for as opposed to directly taking the standard deviation percentage of the internal precision test as uncertainty values were lower than that of the 100 degree set point. It would therefore seem appropriate to opt for an average with higher uncertainty when running Monte Carlo simulations.

## 3.2 Finite element thermal modelling

### 3.2.1 Thermal modelling

#### *Governing equations*

While the target area is a stable basin, the present sedimentation rate is low (approximately ~65m/Ma, determined by Gulson et al. (1990)), and the temporal evolution and convection effect due to sedimentation is ignored in this study. As a result, we solve a stable heat conduction problem as the following form:

$$\nabla \cdot [k(T)\nabla T] + H = 0 \quad (1)$$

#### *Newton's Method*

As thermal conductivity is temperature dependent, a non-linear scheme has to be implemented to solve this problem. Although convergence may be achievable using direct iteration, while thermal conductivity is weakly dependent on temperature. In this study, the partial derivative of thermal conductivity as a function of temperature is simple to approximate, instead we use a more complicated but faster converging Newton scheme.

The initial thermal field for the Newton iteration is found by solving Eq. 1 using thermal conductivity calculated from a constant temperature. Then, while the temperature  $T$  of the previous Newton step is known, the thermal conductivity expressed as  $K$  relative to the temperature used for the next step,  $T + \delta T$  can be approximated as:

$$k(T + \delta T) = k(T) + \frac{\partial k(T)}{\partial T} \delta T \quad (2)$$

The temperature change between steps  $\delta T$  are solved as ( $T$  is known from the previous Newton step):

$$\nabla \cdot \left( \frac{\partial k}{\partial T} \delta T \nabla T \right) + \nabla \cdot [k(T)\nabla \delta T] + \nabla \cdot [k(T) \cdot \nabla T] + H = 0 \quad (3)$$

This solving scheme normally give convergence within ~10 iterations for an error residual of  $2.90655 \times 10^{-6}$  (for thermal profile 1).



## *Deal.II libraries*

To build our own code, an open source finite-element library – deal.ii (<https://www.dealii.org>) is used. It takes care of the details of most finite element codes, such as handling of grid, degrees of freedom, sparse matrices and provides support for different solvers, which helps keep our code manageable. Its dimensionally independent concept and excellent support for adaptive mesh refinement and massively parallel architectures gives great potential for easier future expansion of our code to more complicated 3D thermal models.

### **3.2.2 Computation grid**

When running simulations, the 2D computation domain is 60-180km in length, depending on profile location. Model depth is uniformly set to 12km, and the top surface is based on topography. The mesh is build based on a divided rectangular triangulation (divided to make each mesh cell close to a square), and further globally refined and transformed to fit the topography of the surface. So a global refinement value defines the model resolution. Through trial and error, a global refinement value of 6 (4,096 cells) to 7 (16,384 cells) was decided as it provided an effective compromise for simulation speed and resolution. Simulations with a global refinement value of 6 have a cell size of approximately 200mx200m, while simulations with a global refinement of 7 have a cell size of approximately 100mx100m, effectively quadrupling the resolution, however requiring more time to compute. In practice, an increased resolution rendered by a global refinement value of 7 doesn't seem to have noticeable changes on the results. Simulation time for a global refinement of 6 is very rapid may only take a few seconds, the same goes for a global refinement of 7, usually taking a minute to solve.

Here are two examples of lower global refinements for thermal profile 2, showing the subdivided grid and its impact on the resolution of the model.

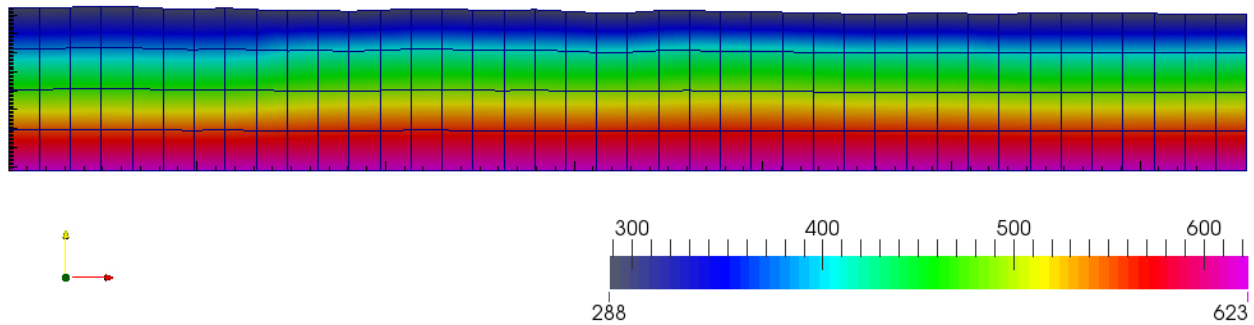


**Figure 3.7 Thermal profile 2 with global refinement of 2, low resolution still captures temperature variation.**

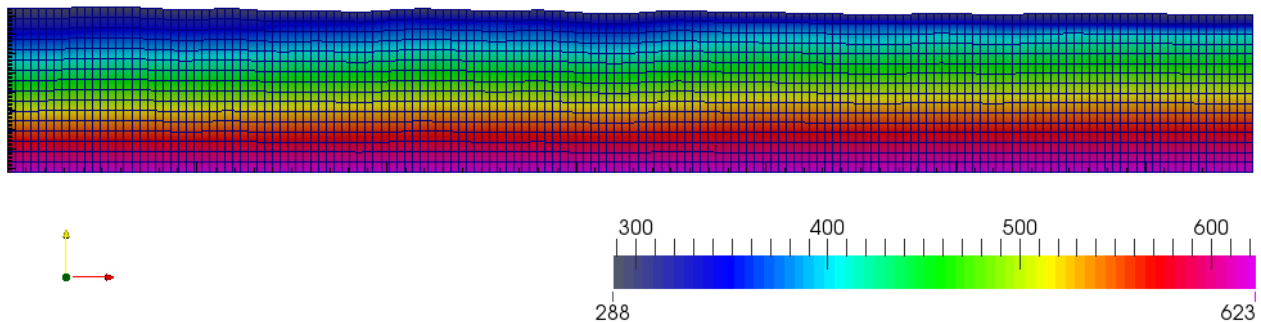


**Figure 3.8 Thermal profile 2 with global refinement of 4, higher resolution showing more detailed temperature variation.**

### 3.2.3 Monte Carlo Method

Monte Carlo simulations were performed utilising a python script. An initial script was written to create directories with respect to the root configuration file, and data files (which contain H and K values, with standard deviations). A total of one thousand directories were generated, all of which have randomly selected thermal conductivity values, from a Gaussian distribution with measured means, and standard deviations. Once a simulation suite has completed, the output from all one thousand directories is compiled into singular plot files. Each plot file shows the mean, while adding and subtracting one standard deviation to show the uncertainty range. A geotherm is taken every 10km along each profile. Extracted geotherms provide a quantitative temperature range useful for determining the thermal arrangement of each profile. Increased iterations (10,000) per simulations are used to determine whether more iterations necessarily mean increased accuracy, as large simulations are computationally expensive and are a time consuming process.

### 3.3 Physical model set-up

The full geological model is constructed as a series of 12 geological profiles, which define the geometry of the major lithological units for all modelled profiles. Heat production values, and variable conductivity are provided for each layer used in the individual models.

#### 3.3.1 Boundary conditions

A surface temperature of 15°C is used, as indicated by Danis et al. (2012). This value is taken from Cull (1989) measurements. A bottom temperature of 350°C at 12km is used, which is the modelled temperature used by Danis et al. (2012) in their models. Side conditions of the model have no heat flow, meaning that boundary temperatures are all accounted for at the top and bottom of the model. Excluding heat flow from side conditions ensures that the model is internally consistent by minimizing edge effects.

#### 3.3.2 Interpolation method

The Lagrange interpolation helps finding the exact value between known data points. Assuming a global refinement value of 6 is used for all simulations, the mesh would be defined by an approximately 200x200m cell size, while a global refinement of 7 would mean a cell size of approximately 100x100m, slight variations would depend on initial profile dimensions. In order to reliably predict fine resolution basin geometry with an adequate lateral resolution, an interpolation method was required. The Lagrange high order interpolating polynomial in this case is used to get a complete distribution between data points for multiple datasets. As a result, the 'void' between real data points is reduced by estimating intermediate data points through 3rd order Lagrange interpolation. A polynomial that passes through and interpolates  $n+1$  coordinates is constructed for all following data points  $(x_0, y_0), (x_1, y_1) \dots (x_3, y_3)$ . A sequential list of values  $(x_0, x_1, x_2, x_3)$  starting from the beginning of the profile are used to define interpolating polynomials, where for instance:

$$y = jx^3 + kx^2 + mx + c$$

In this case: j, k, m, and c are constants associated with initial values the polynomial was calculated from. This polynomial would intersect all points defined by the interpolating functions.

### 3.3.3 Spatial information

The basin geometry used to characterise the geothermal models generated in this study has been taken from the raw data component of the gravity modelling undertaken by Danis et al. (2011). The model is divided into a total of 12 profiles, which extend laterally W-E along the length of the Sydney Basin. As a result, all profiles vary in size. This method was opted for as it retains consistency with models constructed by Danis et al. (2011/2012) and serves as a useful platform for direct comparison. The traverse length of each profile was extracted from published figures in Danis et al. (2011/2012) by digitizing each respective longitude and latitude. Once the traverse length is established, the following equation is used to provide the distance in meters from the western most point of the Sydney Basin to the eastern most point, which would be determined by its coastal outline.

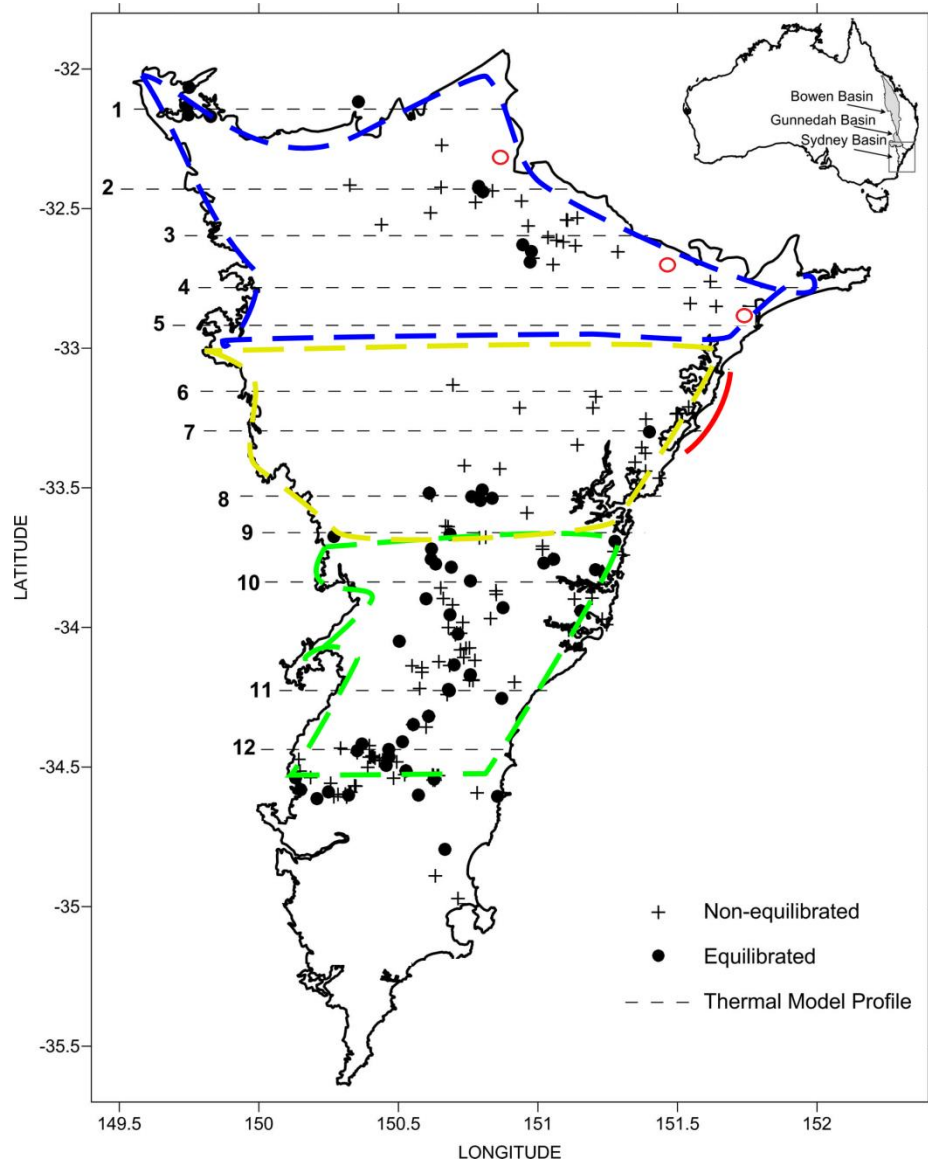
All profiles have known latitudes, which is transformed into 2D Cartesian form. We calculate the horizontal coordinate as:

$$x = R_e \cos\left(\frac{lat}{180} * \pi\right) * \frac{lon1 - lon0}{180} * \pi$$

$R_e$  is the radius of the earth,  $lat$  is the latitude of the profile,  $lon0$  and  $lon1$  are the longitude of the target and starting points respectively.

### 3.3.4 Profile geometry

All profiles have 4 layers consisting of a Triassic sedimentary layer, a Permian coal layer, a Carboniferous volcanics layer and a Carboniferous Basement layer. Profiles 1-6 have the most complex geometry with one additional 'Greta' coal layer overlain by the Permian coal layer. The base of the sedimentary layer is defined down to the top of the volcanics layer, and coal layer(s) intermittently reside within the sedimentary layer. Bottom of the basement is not depicted in following profiles; however simulations assume a basement limit of 12 km. The following figures (Profiles 1 to 12) are orientated in an EW fashion.



**Map 1: Plan view of the Sydney Basin with coordinates, showing location of profile lines 1 to 12, adapted from Danis et al. (2012). Blue, yellow and green lines show the outline of different basement types, including Gulgong, Bathurst and Wyangala respectively. Red circles show coal sampling locations, and the red line shows the sediments sampling locations.**

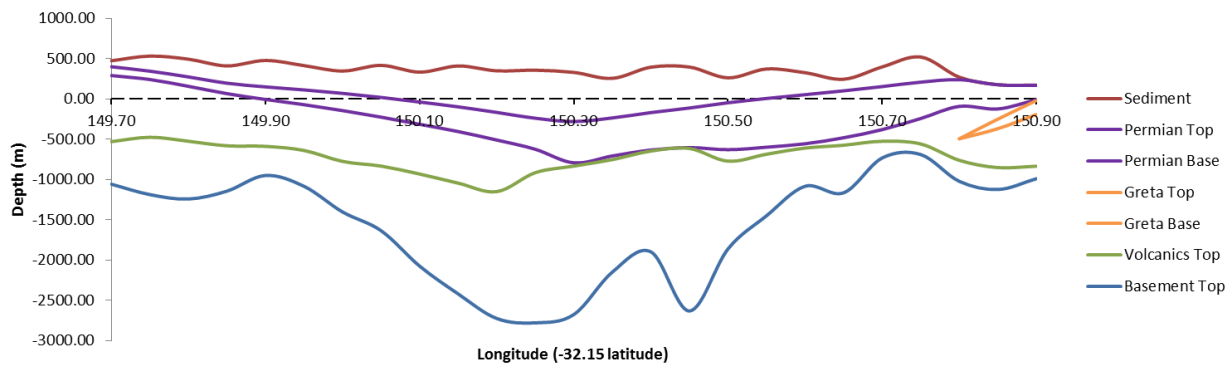


**Figure 3.9 Profile 1: latitude -32.15, longitude 149.70-150.90**

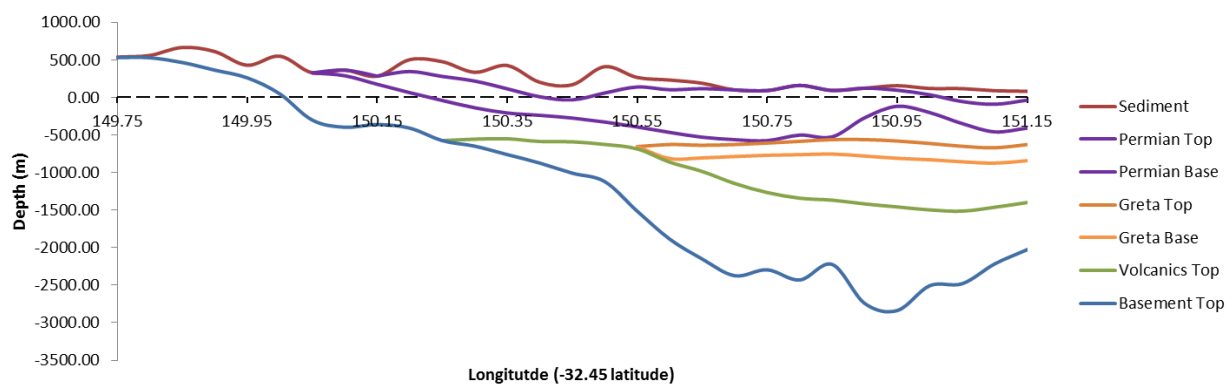


**Figure 3.10 Profile 2: latitude -32.45, longitude 149.75-151.15**

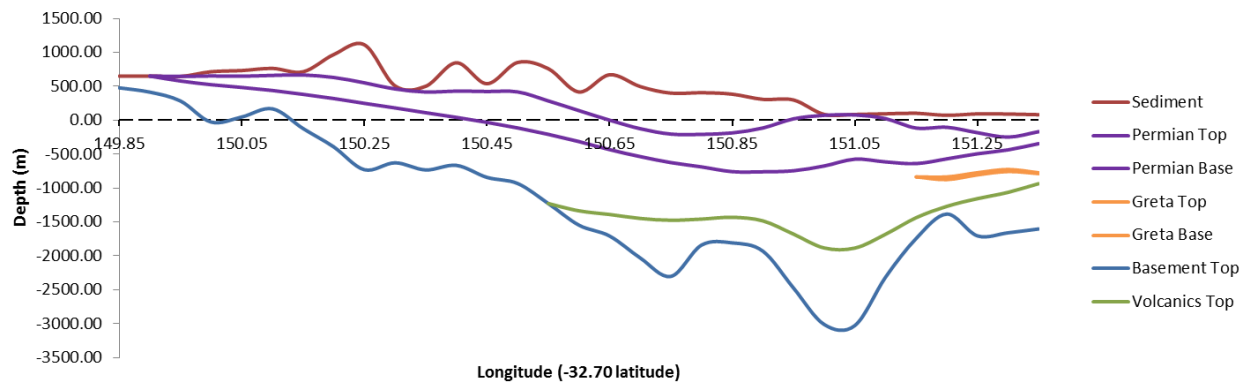


**Figure 3.11 Profile 3: latitude -32.70, longitude 149.85-151.35**

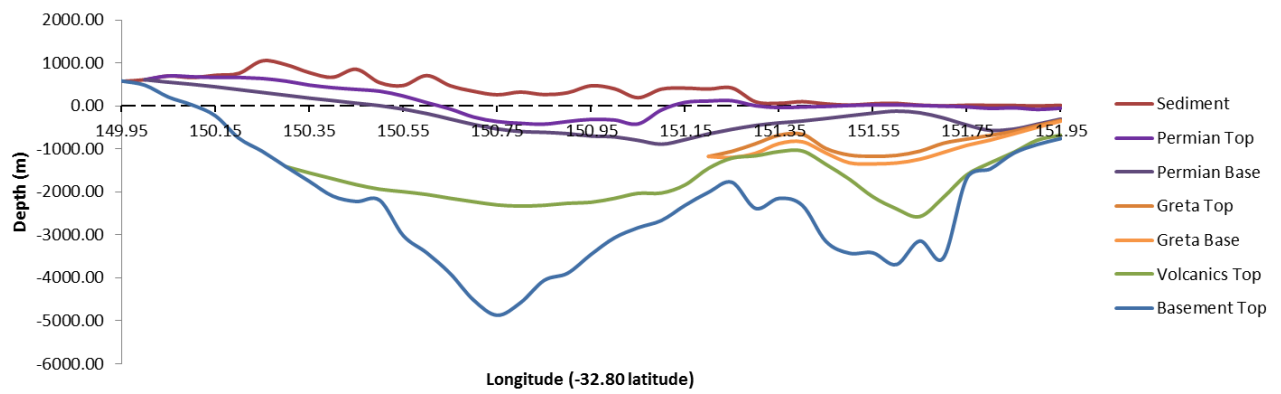


**Figure 3.12 Profile 4: latitude -32.80, longitude 149.95-151.95**

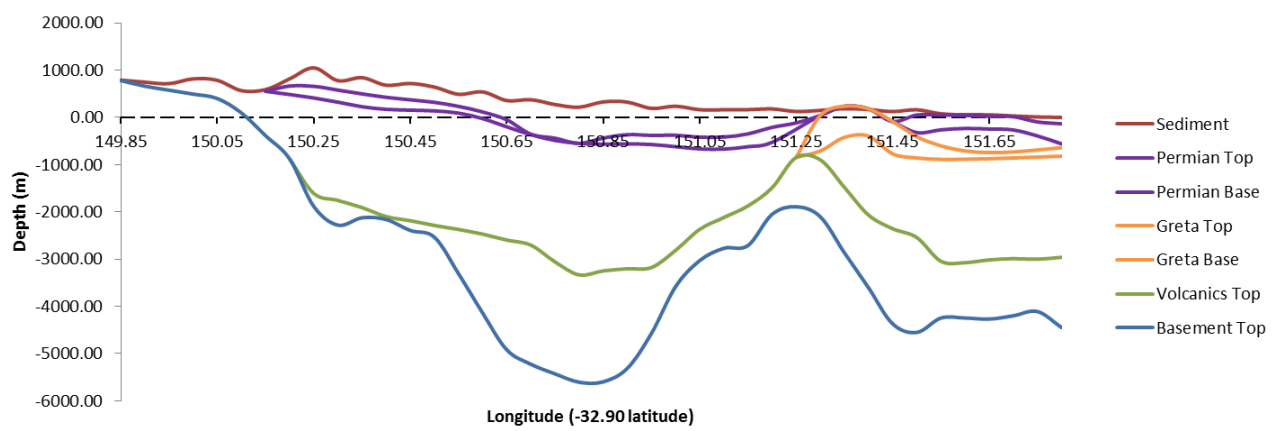


**Figure 3.13 Profile 5: latitude -32.90, longitude 149.85-151.80**

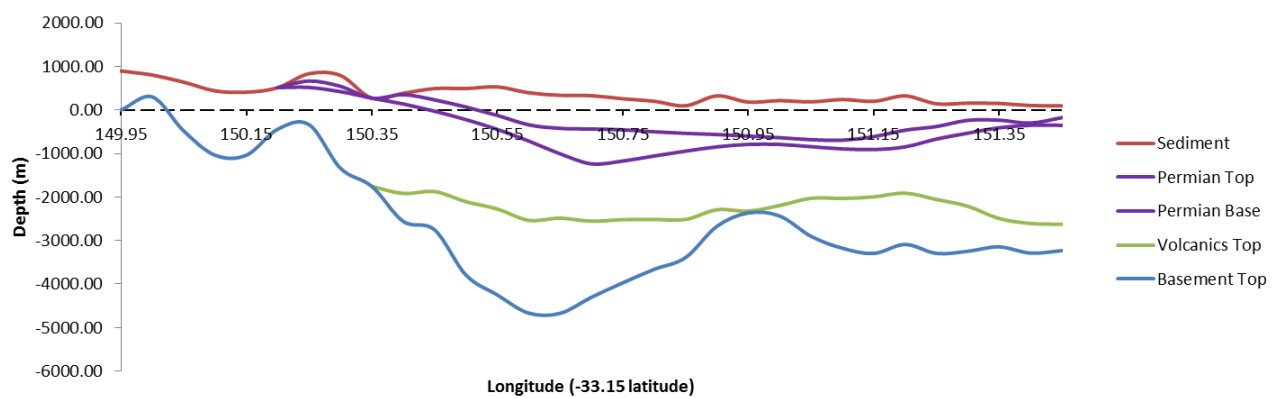


**Figure 3.14 Profile 6: latitude -33.15, longitude 149.95-151.45**

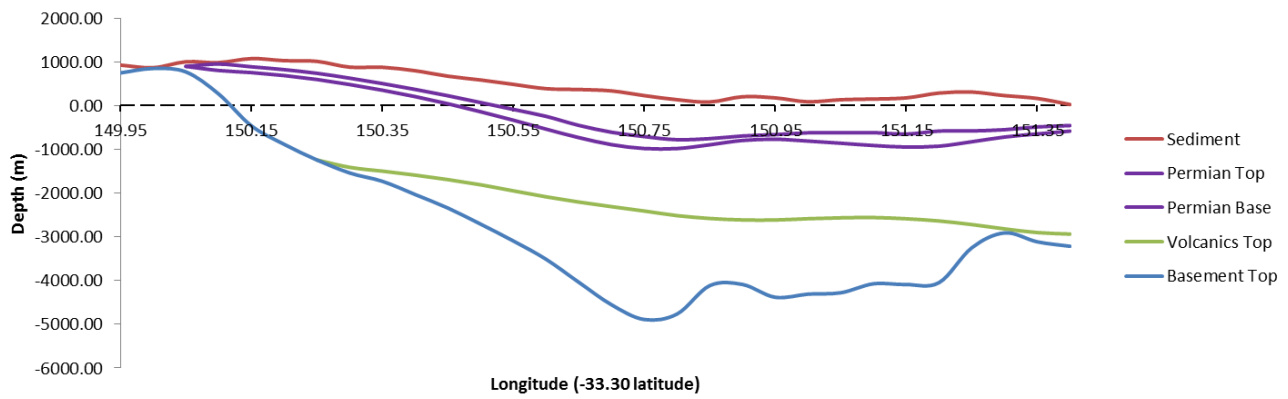


**Figure 3.15 Profile 7: latitude -33.30, longitude 149.95-151.40**

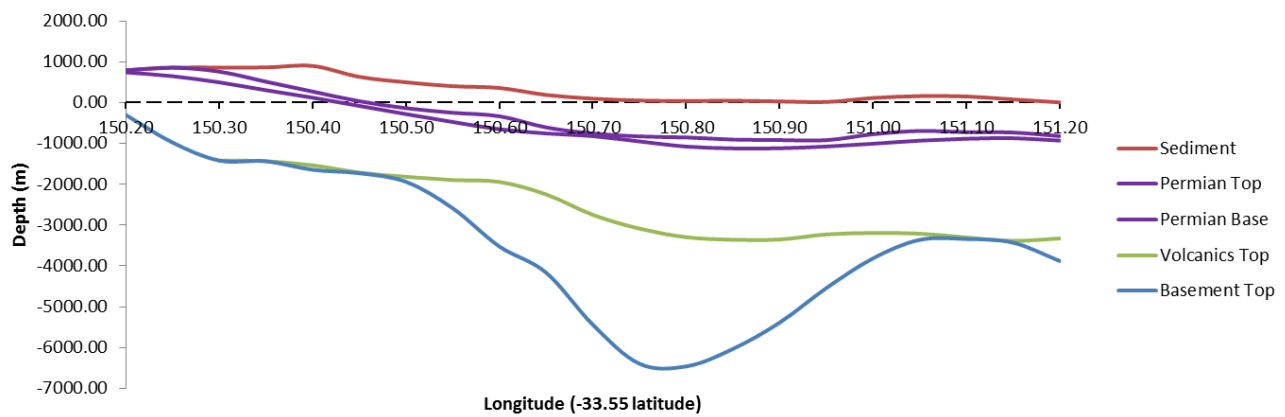


**Figure 3.16 Profile 8: latitude -33.55, longitude 150.20-151.20**

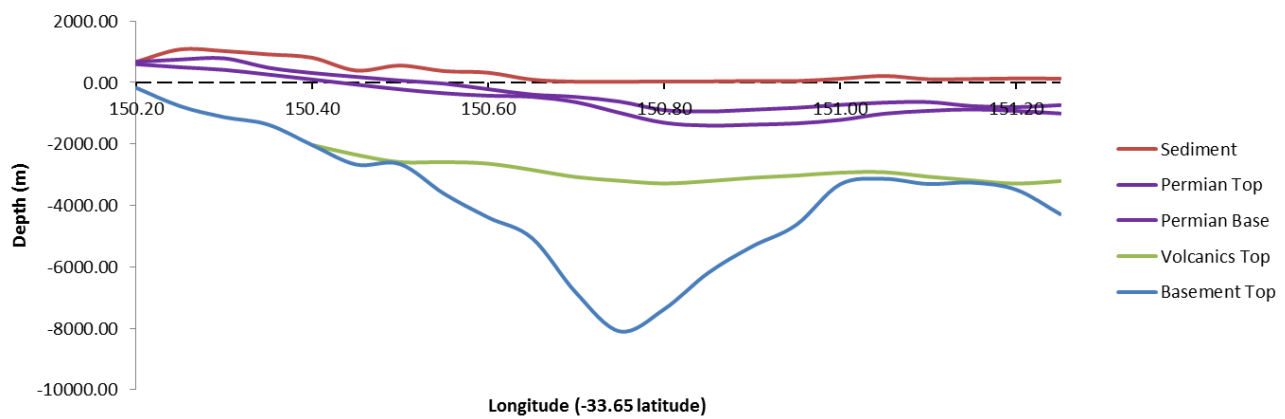


**Figure 3.17 Profile 9: latitude -33.65, longitude 150.20-151.25**



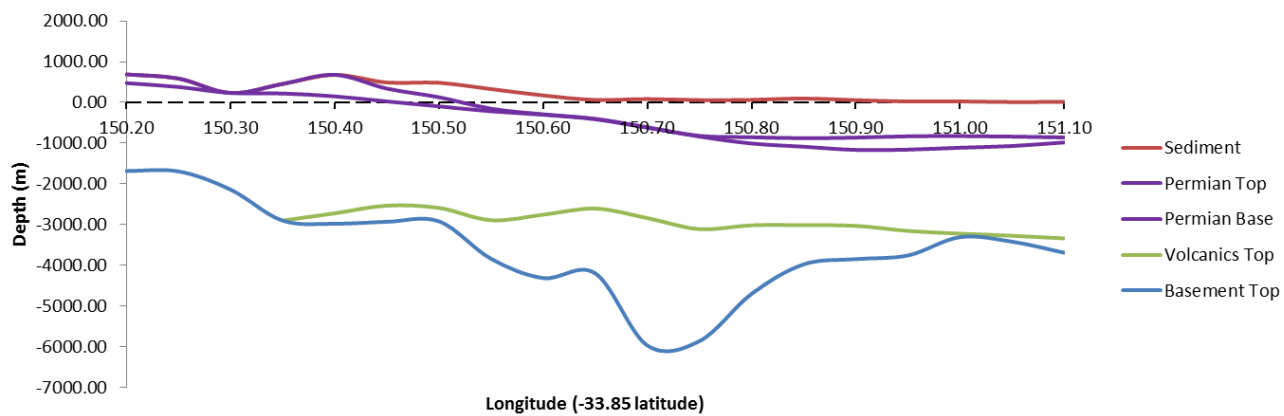


**Figure 3.18 Profile 10: latitude -33.85, longitude 150.20-151.10**

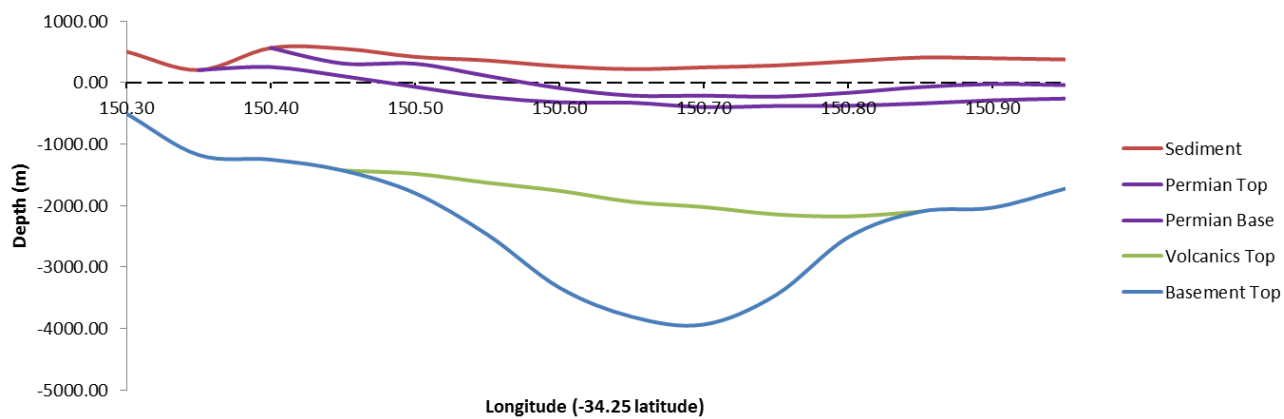


**Figure 3.19 Profile 11: latitude -34.25, longitude 150.30-150.95**

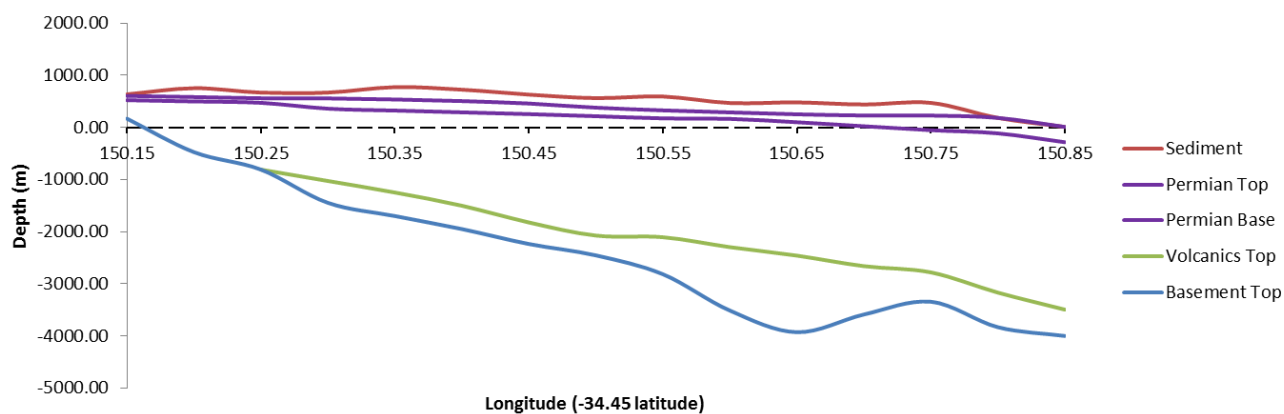


**Figure 3.20 Profile 12: latitude -34.45, longitude 150.15-150.85**

### 3.3.5 Heat production values

Heat production values have been taken from two prominent sources. Facer (1980) provides a short list of packages from the Southern Coalfields in NSW and Blevin et al. (2010). Vila et al. (2010) offers a range of values for common lithological groups, but does not offer site specific values that are provided by Facer (1980) and Blevin (2010). Approximated heat production values of Triassic sedimentary rocks, igneous intrusions / dykes that have been identified as intrusions of coal measures, and Permian coal measure sedimentary rocks were sampled by Facer (1980). A number of the Permian samples have been recognised as inter-seam clastic rocks with varying heat production values, as a result, this represents an average between the organic and non-organic component of Permian sedimentary packages.

Although reported values are based on a limited number of samples and that it is assumed heat production values remain constant within defined layers or packages, they provide a general idea of the large scale heat production of pre-defined lithological packages studied in this project. Heat production values were collected via XRF (X-ray fluorescence) analysis of K and Th and U via NAA (Neutron activation analysis).

A more recent study by Vila et al. (2010) explores the radiogenic heat production variability of common lithological groups. A large compilation of heat production measurements were provided, showing a mean and percentile difference of heat production values. Reported values vary significantly with standard deviations in some instances exceeding the mean. It was shown by Vila et al. (2010) that it is difficult to approximate and nominate specific values to a group of lithologies. Heat production values vary with location, and in order to keep value distributions manageable - taking the mean is established to be the most effective approximation, and provides a relatively realistic representation of true values.

Blevin et al. (2010), is dealing with a relatively large dataset, consisting of a highly specific set of basement rocks. Measured heat production values of the Sydney Basin basement, the igneous groups measured, classified by age, are the Gulgong, Bathurst and Oberon Granites which represent a large number of the Lachlan Fold

belt Carboniferous granitoids. At the current resolution of simulations, heat production is averaged across all layers for simplicity, including basement values.

Facer's (1980) referenced specimens are close to our area of interest, so we adopt these estimates, taking into account the uncertainty in the measurements. As a result, the following values have been used, in conjunction with Blevin's et al. (2010) basement estimates.

<i>Layer number</i>	<i>Heat production value (<math>\mu\text{Wm}^{-3}</math>)</i>
Layer 0 (sediment)	1.1
Layer 1 (volcanics)	0.87
Layer 2 (basement)	3.3
Coal layer 1	2.1
Coal layer 2	3.1

## 4. Results

### 4.1 Thermal conductivity measurements

Thermal conductivity values used for this study are shown in table 4.1 and 4.2. These include basement thermal conductivities, compiled from Evans's (2013) Lachlan Fold Belt Granites measurements, and new measurements on Sydney Basin sediments. The Lachlan Belt Granites are representative of a number of granitic bodies which extend down to the Sydney Basin basement (Evans 2013). The thermal conductivity of each profile was calculated by taking the average of surrounding granites corresponding to the latitude of each thermal profile. The thermal conductivity, for a given temperature, of the Triassic sediment, coal measures and volcanics was assumed to remain constant across all thermal profiles as these measurements do not possess the same degree of coverage as the granites.

Temperature dependent thermal conductivity of sediment and coal measures measurements were taken in 2014 as part of this study. Volcanics thermal conductivities are taken as recommended temperature dependent estimates taken from Danis et al. (2012).

Page left blank

Temp (°C) and s.d.	20	s.d.	50	s.d.	100	s.d.	150	s.d.	200	s.d.	250	s.d.	300	s.d.
Basement layer 1-2	2.765	0.186	2.533	0.155	2.392	0.124	2.253	0.125	2.073	0.115	1.955	0.109	1.849	0.103
Basement layer 3-5	1.444	0.097	1.414	0.061	1.348	0.025	1.291	0.013	1.221	0.013	1.182	0.012	1.141	0.012
Basement layer 6-7	3.028	0.203	2.886	0.169	2.657	0.134	2.465	0.125	2.225	0.114	2.078	0.105	1.963	0.099
Basement layer 8	2.652	0.178	2.457	0.134	2.329	0.091	2.204	0.077	2.052	0.072	1.966	0.069	1.867	0.065
Basement layer 9	2.631	0.177	2.434	0.121	2.276	0.065	2.142	0.053	1.995	0.050	1.907	0.048	1.810	0.045
Basement layer 10	2.910	0.195	2.647	0.140	2.446	0.085	2.277	0.075	2.097	0.069	1.979	0.065	1.863	0.061
Basement layer 11	3.484	0.234	3.151	0.159	2.791	0.084	2.533	0.114	2.301	0.104	2.128	0.096	1.998	0.090
Basement layer 12	3.078	0.207	2.781	0.177	2.602	0.147	2.446	0.141	2.244	0.129	2.105	0.121	1.990	0.114
Temp (°C) and s.d.	20	s.d.	50	s.d.	100	s.d.	150	s.d.	200	s.d.	250	s.d.	300	s.d.
Sediment layer	1.088	0.073	1.072	0.063	1.056	0.054	1.021	0.055	0.994	0.054	0.989	0.053	0.994	0.054
Permian coal layer	0.692	0.046	0.676	0.044	0.684	0.041	0.672	0.040	0.679	0.040	0.719	0.043	0.788	0.047
Greta coal layer	0.376	0.025	0.308	0.020	0.279	0.014	0.229	0.012	0.254	0.013	0.356	0.018	0.452	0.023
Volcanics layer	3.000	1.000	3.000	0.750	2.500	0.500	2.500	0.500	2.500	0.500	2.500	0.500	2.250	0.250

**Table 4.1 Thermal conductivity measurements with standard deviations**

The values used for constant thermal conductivities are shown in the following table:

<i>Geological layer</i>	<i>Thermal conductivity (W/mK)</i>
Sediments	2.0
Volcanics	3.0
Basement	3.0
Permian coal	0.3
Greta coal	0.3

**Table 4.2 Thermal conductivity values used for constant thermal conductivity thermal models, values used by Danis, et al. (2012)**

**Basement thermal conductivity values, compiled from Evans (2013)**

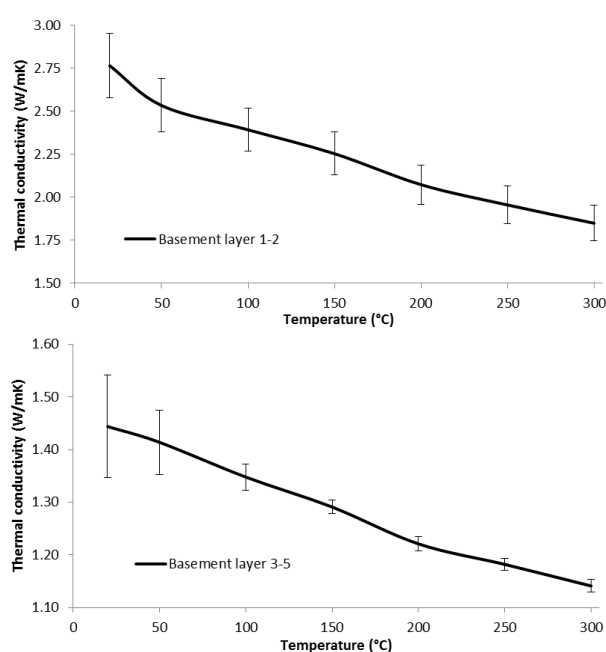


**Figure 4.1.1 Basement layer thermal conductivity for profiles 1 and 2, with standard deviation shown. Values depict the Gulgong granite. Figure 4.1.2 Basement layer thermal conductivity for profiles 2 and 3, with standard deviation shown. Values depict the Gulgong granite.**

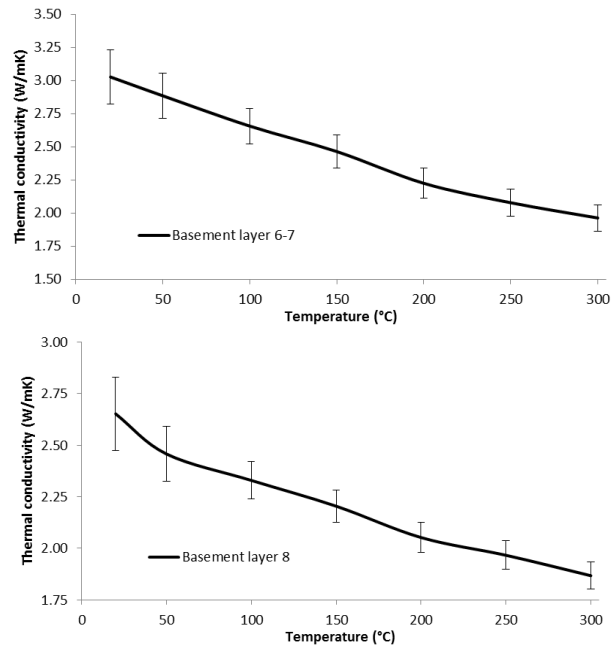


**Figure 4.1.3 Basement layer thermal conductivity for profiles 6 and 7, with standard deviation shown. Values depict the Bathurst granite. Figure 4.1.4 Basement layer thermal conductivity for profile 8, with standard deviation shown. Values depict the Bathurst granite.**

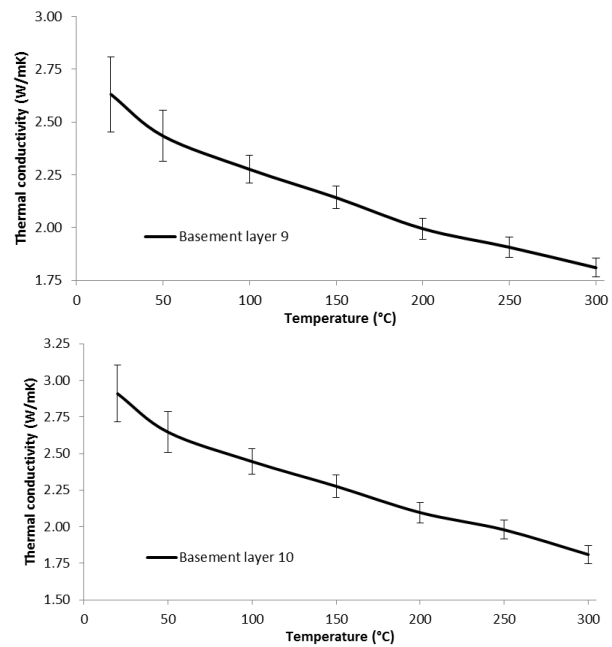


**Figure 4.1.5 Basement layer thermal conductivity for profile 9, with standard deviation shown. Values depict the Bathurst granite. Figure 4.1.6 Basement layer thermal**

**conductivity for profile 10, with standard deviation shown. Values depict the Bathurst and Oberon granite.**

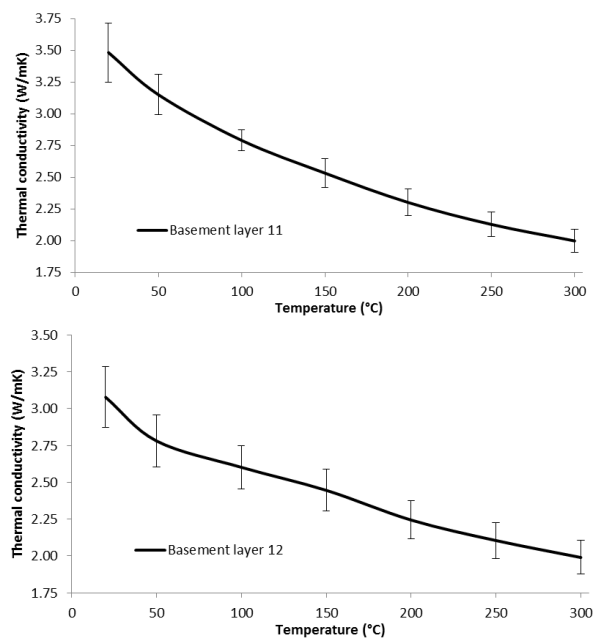


**Figure 4.1.7 Basement layer thermal conductivity for profile 11, with standard deviation shown. Values depict the Wyangala granite. Figure 4.1.8 Basement layer thermal conductivity for profile 12, with standard deviation shown. Values depict the Oberon granite.**



## Sediment, coal measures and volcanics thermal conductivity measurements

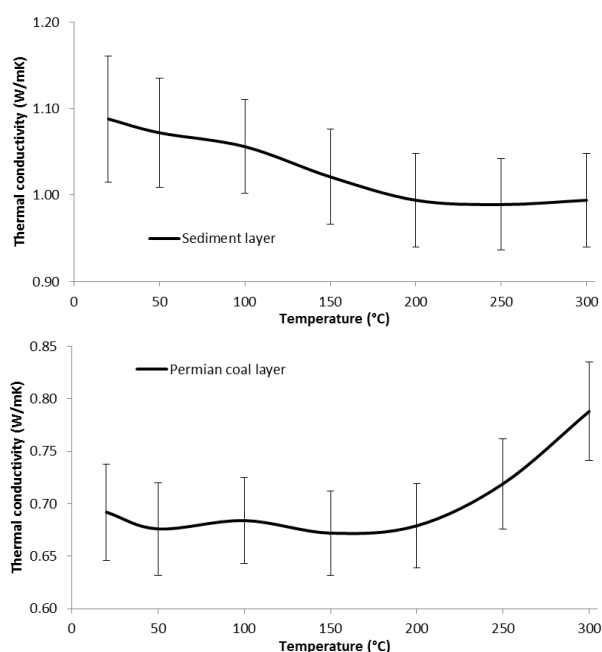


**Figure 4.1.9 Sediment (fine to coarse grained Triassic sandstone) thermal conductivity with standard deviation shown. Figure 4.1.10 Permian coal thermal conductivity with standard deviation shown.**

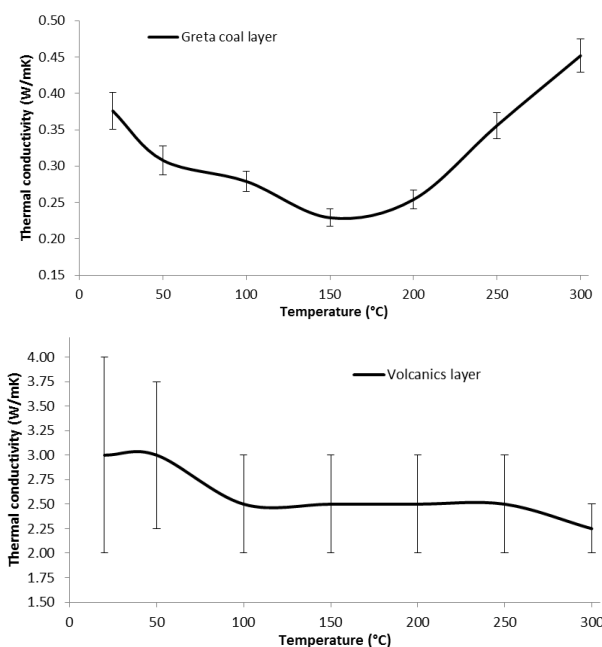


**Figure 4.1.11 Greta coal thermal conductivity with standard deviation show. Figure 4.1.12 Volcanics thermal conductivity with standard deviation shown. This layer represents Carboniferous rift volcanics in the models.**

Thermal conductivity of basement values all follow a reducing trend, where measurements reveal a decrease in thermal conductivity with temperature. Coal and sediment values also have quite well constrained standard deviations based on internal precision values. The volcanics layer on the other hand, displays the largest uncertainties. Thermal conductivity of the Sydney Basin Carboniferous volcanics were estimated by Danis et al. (2010), so we attributed the volcanics a large uncertainty range as those thermal conductivities were not experimentally obtained, as no Carboniferous volcanics of the Sydney Basin have been experimentally studied in terms of their thermal conductivity. As previously stated by Clauser (1995), thermal conductivity generally decreases with temperature. This rule is consistent with values presented here, except for the thermal conductivity of coal. It has been demonstrated by Rezaei et al. (2000) that the thermal conductivity of coal ash actually increases with temperature from 200 to 800°C. Thermal conductivity measurements in this study are taken from 20 to 300°C, however this increasing trend correlates with high temperature measurements (200-300°C). The Permian and Greta coal measures have been given different thermal conductivity values, as Permian coal seams appear as lenses within sediments, as described in the geological background section (Figure 1.2). Permian coal thermal conductivity values were averaged between the Newcastle, Tomago and Whittingham coal measures and the Triassic Sydney Basin sediments, while the Greta coal thermal conductivity is purely representative of coal.

A benchmark test is used to confirm that our thermal models work by applying very simple constraints. A linear geometry and a uniform thermal conductivity of 1W/mK (any number would do) on the entire profile is used to create a linear geotherm. The resulting temperature distribution is hence entirely dependent on the presence and absence of internal heating rates and boundary conditions. A global refinement of 7 is used.

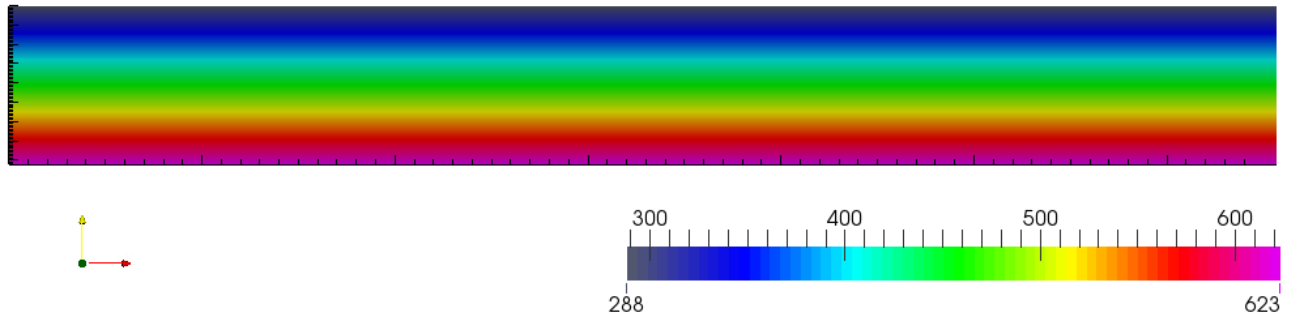


**Figure 4.1.13 Benchmark test with boundary conditions – 15°C and 350°C for top and bottom respectively. Here the temperature distribution is entirely dependent on boundary condition without any internal heating.**

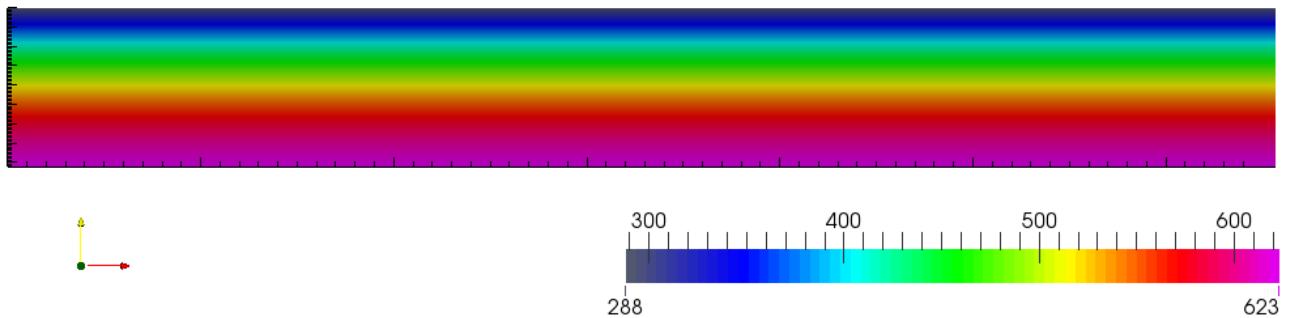


**Figure 4.1.14 Benchmark test with boundary conditions – 15°C and 350°C for top and bottom respectively. Here the temperature distribution is both dependent on boundary conditions and internal heating.**

Benchmarks tests show a response to boundary conditions and internal heating rate. Since this response is linear, a difference in the thermal field is going to be due to thermal conductivity variation and profile geometry.

## 4.2 Constant thermal conductivity model

Temperature dependent thermal profiles and non-temperature dependent thermal profiles are independently shown with a 150°C isotherm for direct comparison. These profile locations are displayed on Figure 3.9 to 3.20, and the constant thermal conductivity values are from Table 4.1.

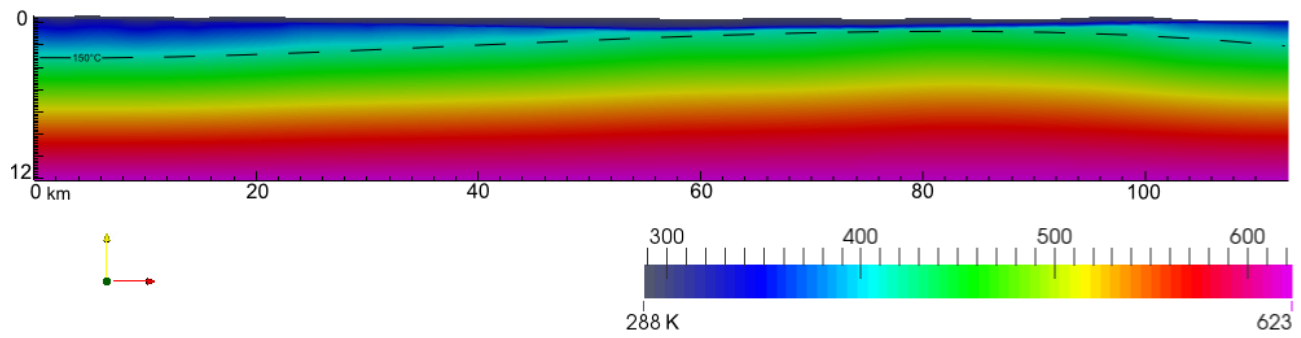


**Figure 4.2.1 Thermal profile 1 (non-temperature dependent): featuring 150° C/423° K isotherm, temperature scale in degrees Kelvin.**

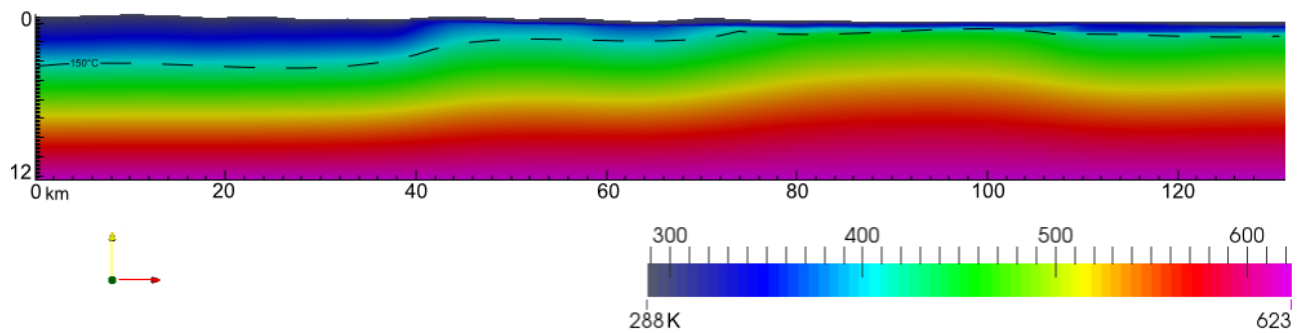


**Figure 4.2.2 Thermal profile 2 (non-temperature dependent): featuring 150° C/423° K isotherm, temperature scale in degrees Kelvin.**

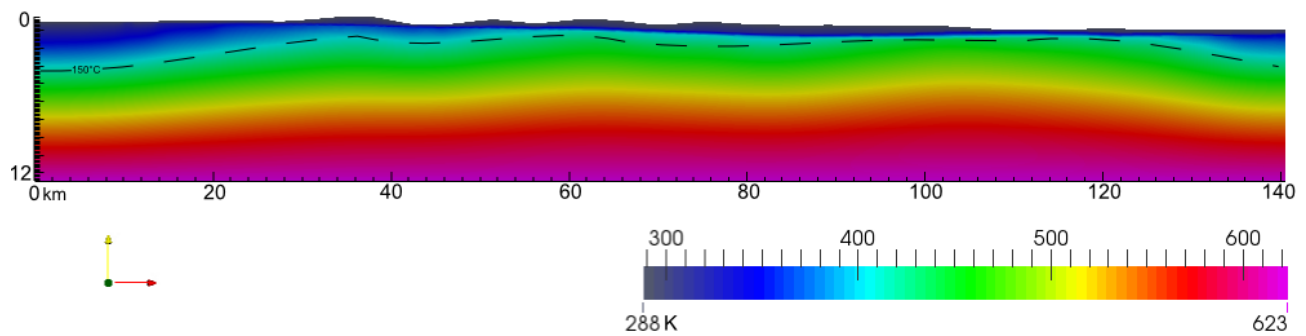


**Figure 4.2.3 Thermal profile 3 (non-temperature dependent): featuring 150° C/423° K isotherm, temperature scale in degrees Kelvin**

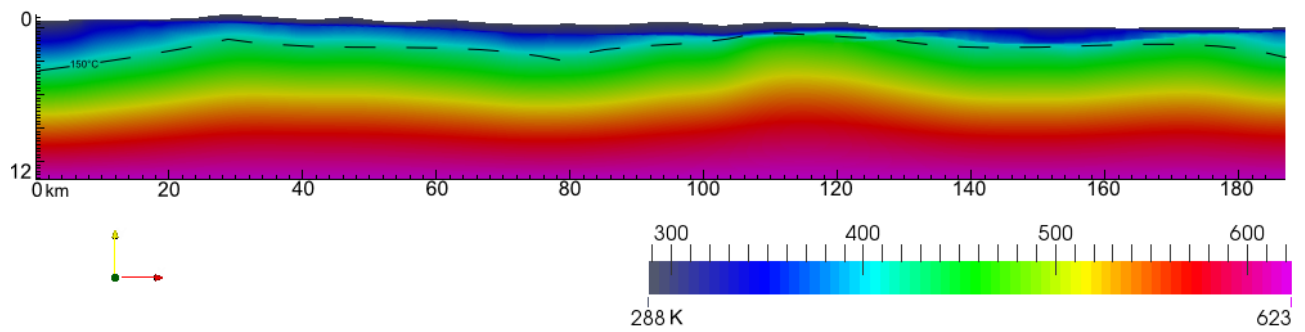


**Figure 4.2.4 Thermal profile 4 (non-temperature dependent): featuring 150°C/423° K isotherm, temperature scale in degrees Kelvin**

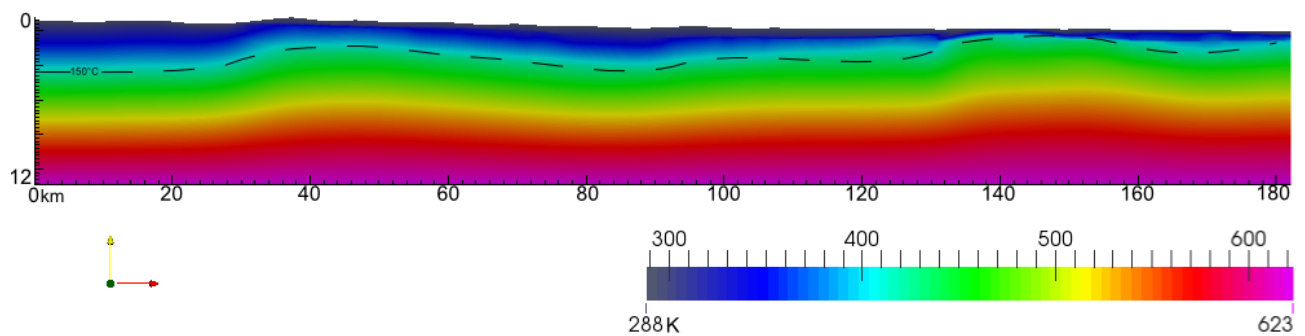


**Figure 4.2.5 Thermal profile 5 (non-temperature dependent): featuring 150°C/423° K isotherm, temperature scale in degrees Kelvin**

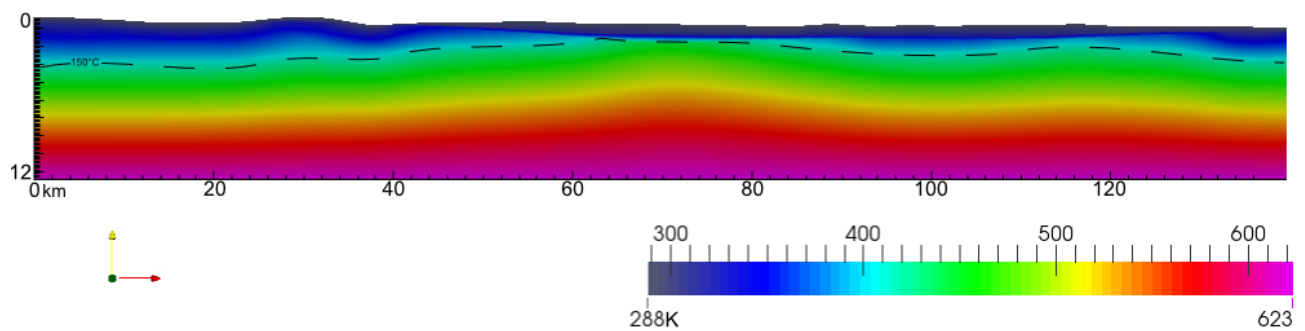


**Figure 4.2.6 Thermal profile 6 (non-temperature dependent): featuring 150°C/423° K isotherm, temperature scale in degrees Kelvin**

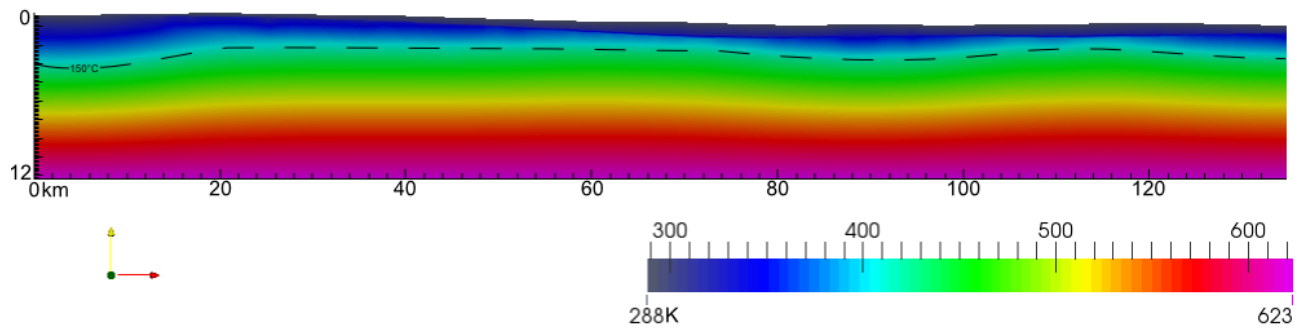


**Figure 4.2.7 Thermal profile 7 (non-temperature dependent): featuring 150° C/423° K isotherm, temperature scale in degrees Kelvin**

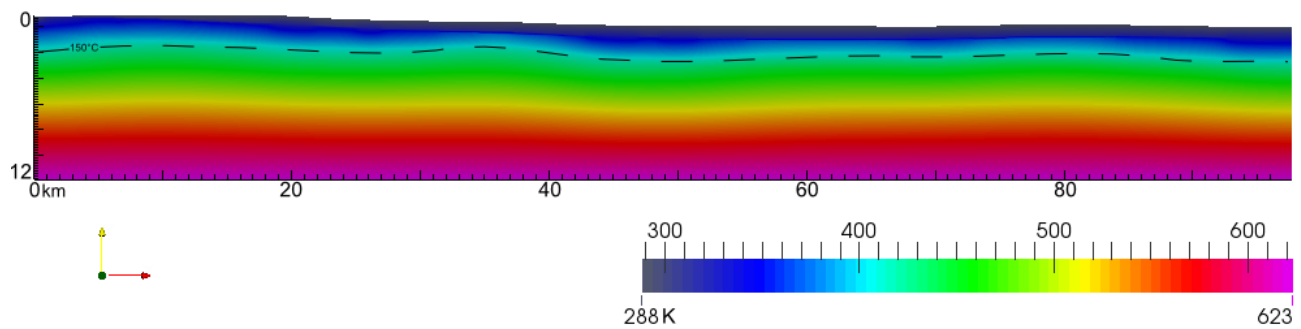


**Figure 4.2.8 Thermal profile 8 (non-temperature dependent): featuring 150° C/423° K isotherm, temperature scale in degrees Kelvin**

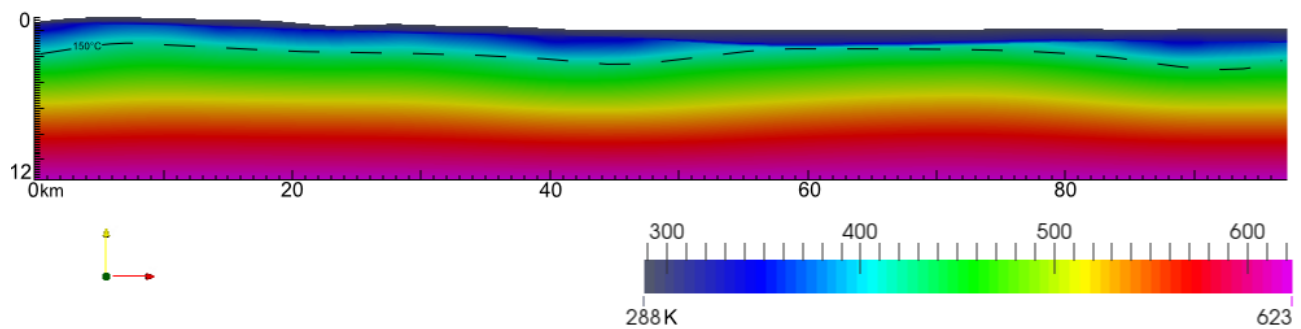


**Figure 4.2.9 Thermal profile 9 (non-temperature dependent): featuring 150° C/423° K isotherm, temperature scale in degrees Kelvin**

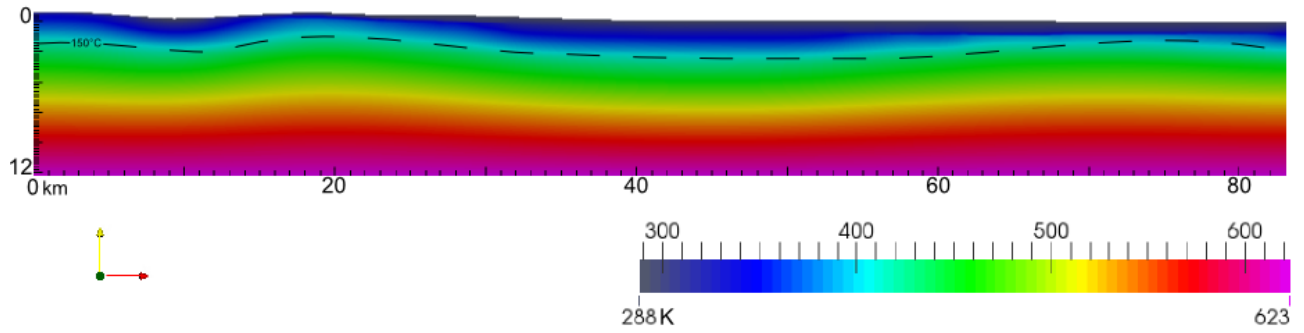


**Figure 4.2.10 Thermal profile 10 (non-temperature dependent): featuring 150°C/423°K isotherm, temperature scale in degrees Kelvin**

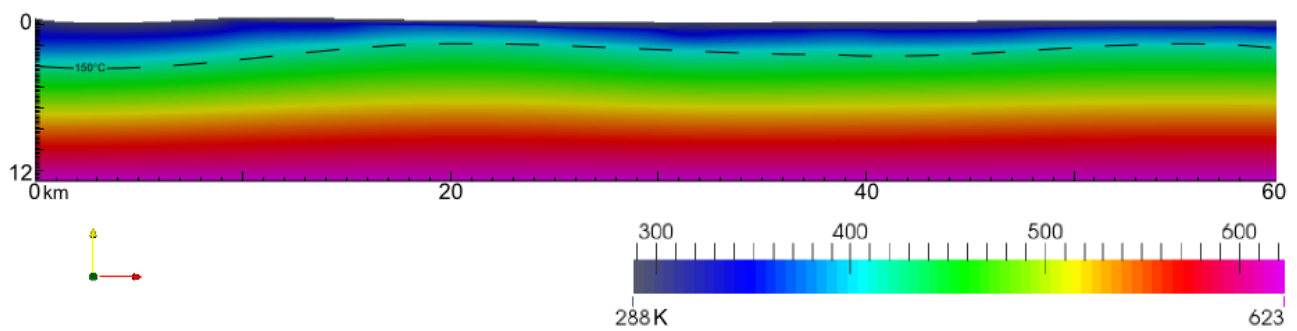


**Figure 4.2.11 Thermal profile 11 (non-temperature dependent): featuring 150°C/423°K isotherm, temperature scale in degrees Kelvin**

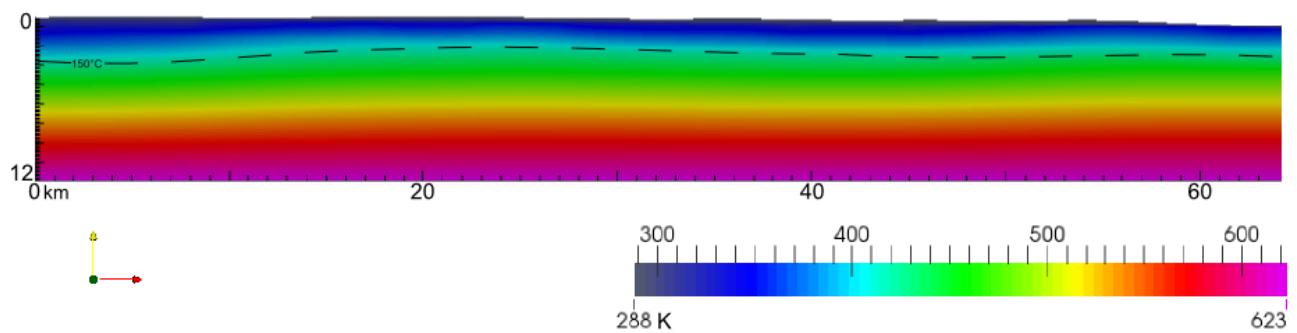


**Figure 4.2.12 Thermal profile 12 (non-temperature dependent): featuring 150°C/423°K isotherm, temperature scale in degrees Kelvin**

### 4.3 Temperature dependent thermal conductivity model

The following thermal profiles are for the same locations as the preceding section, as shown in Figures 3.9 to 3.20. However, here we are utilizing the temperature-dependent conductivity curves derived experimentally from section 4.1, fitted with a fourth-order polynomial.

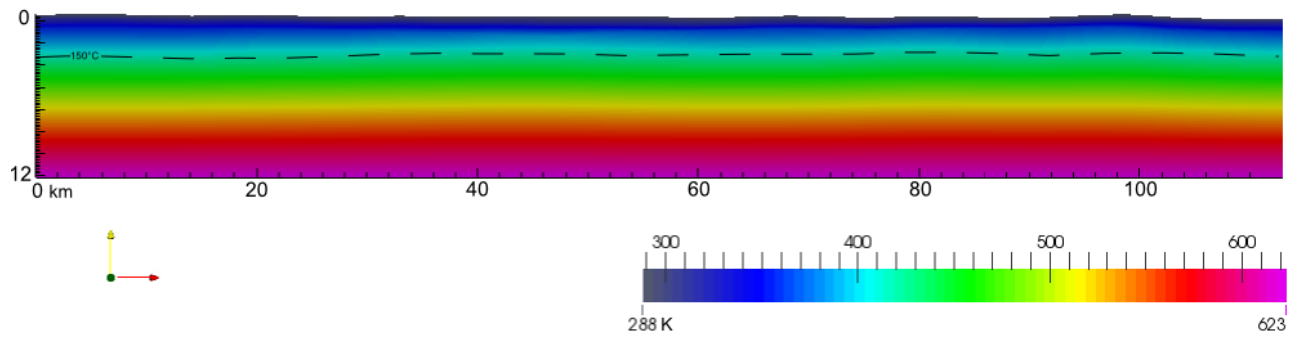


**Figure 4.3.1 Thermal profile 1 (temperature dependent): featuring 150° C/423° K isotherm, temperature scale in degrees Kelvin**

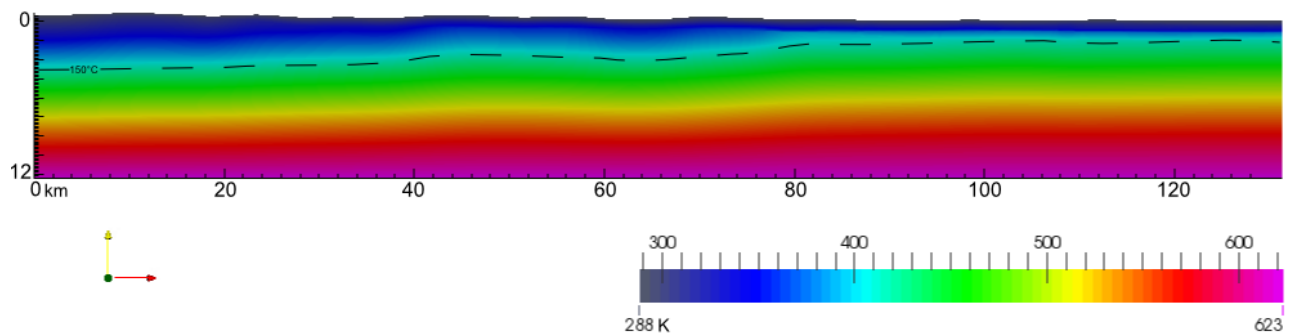


**Figure 4.3.2 Thermal profile 2 (temperature dependent): featuring 150° C/423° K isotherm, temperature scale in degrees Kelvin**

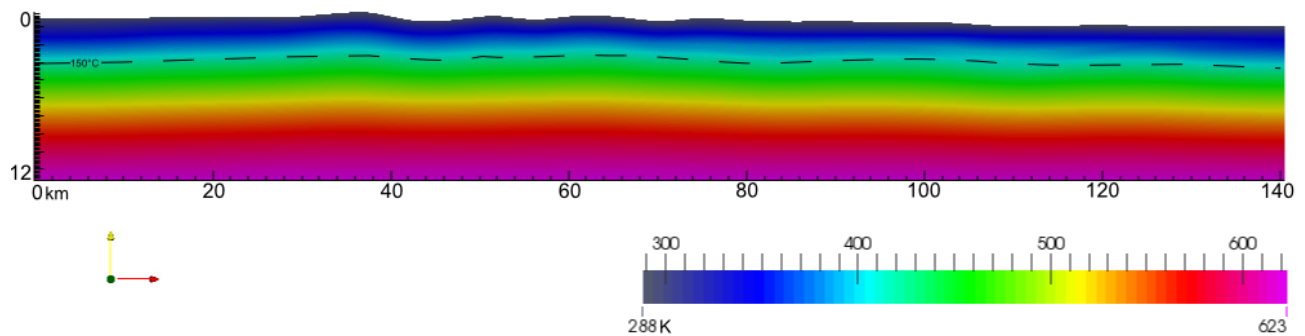


**Figure 4.3.3 Thermal profile 3 (temperature dependent): featuring 150° C/423° K isotherm, temperature scale in degrees Kelvin**



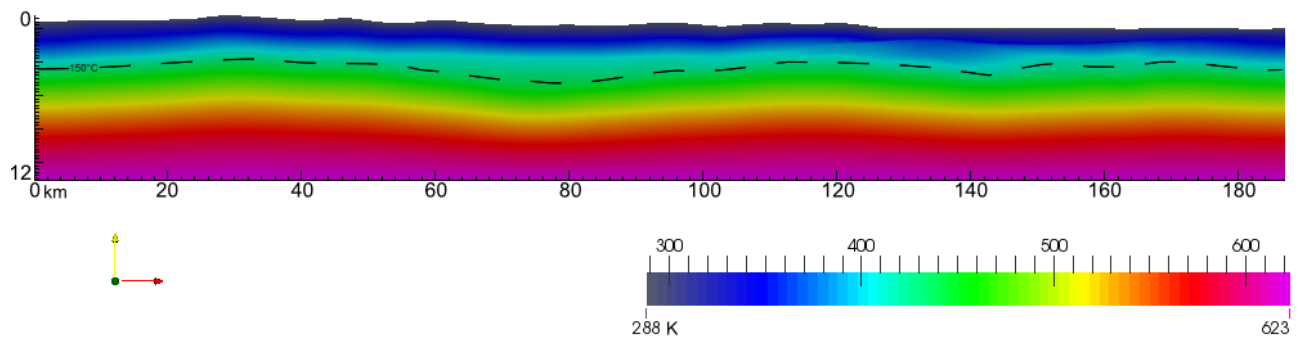


**Figure 4.3.4 Thermal profile 4 (temperature dependent): featuring 150° C/423° K isotherm, temperature scale in degrees Kelvin**

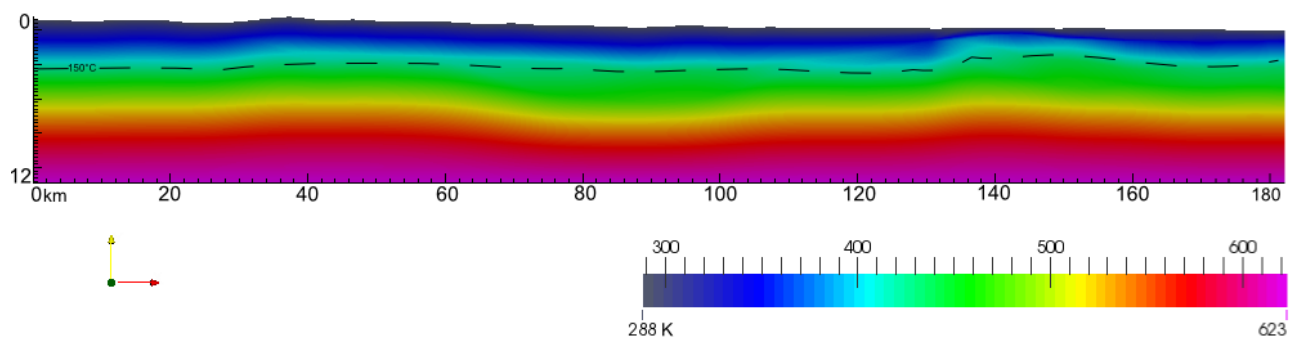


**Figure 4.3.5 Thermal profile 5 (temperature dependent): featuring 150° C/423° K isotherm, temperature scale in degrees Kelvin**

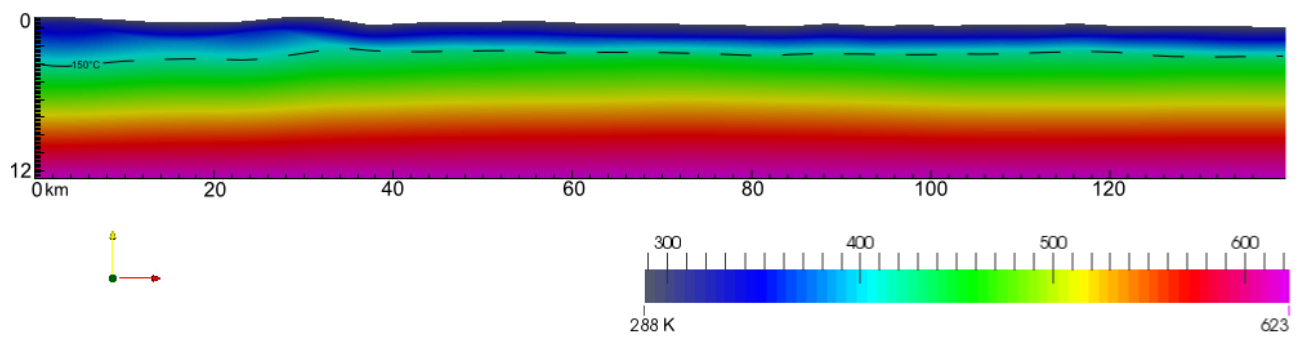


**Figure 4.3.6 Thermal profile 6 (temperature dependent): featuring 150° C/423° K isotherm, temperature scale in degrees Kelvin**

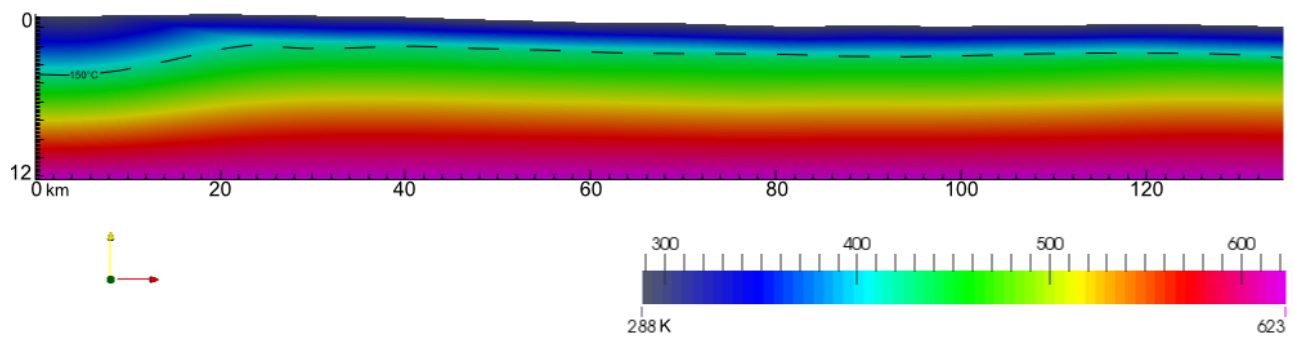


**Figure 4.3.7 Thermal profile 7 (temperature dependent): featuring 150° C/423° K isotherm, temperature scale in degrees Kelvin**

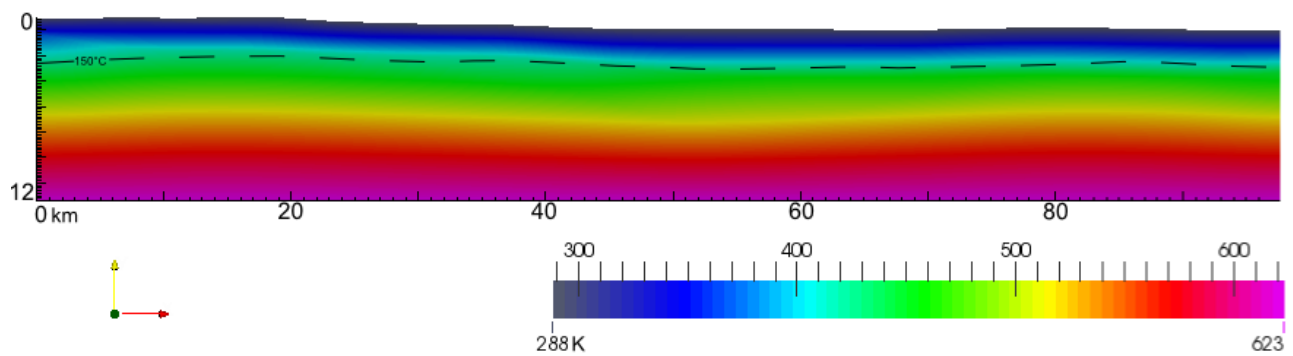


**Figure 4.3.8 Thermal profile 8 (temperature dependent): featuring 150° C/423° K isotherm, temperature scale in degrees Kelvin**

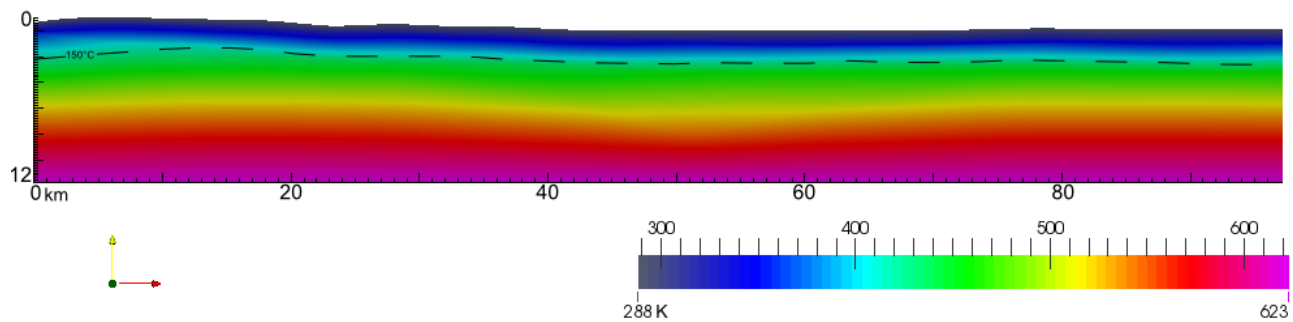


**Figure 4.3.9 Thermal profile 9 (temperature dependent): featuring 150° C/423° K isotherm, temperature scale in degrees Kelvin**

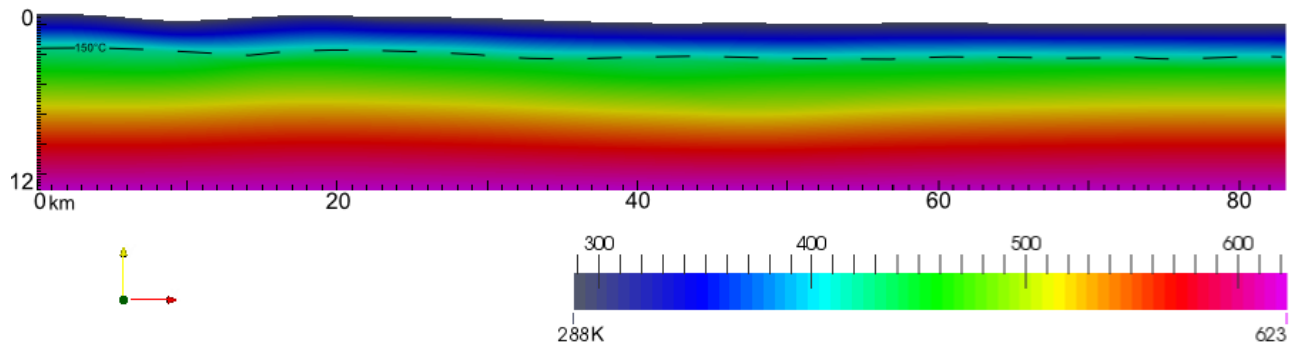


**Figure 4.3.10 Thermal profile 10 (temperature dependent): featuring 150°C/423°K isotherm, temperature scale in degrees Kelvin**

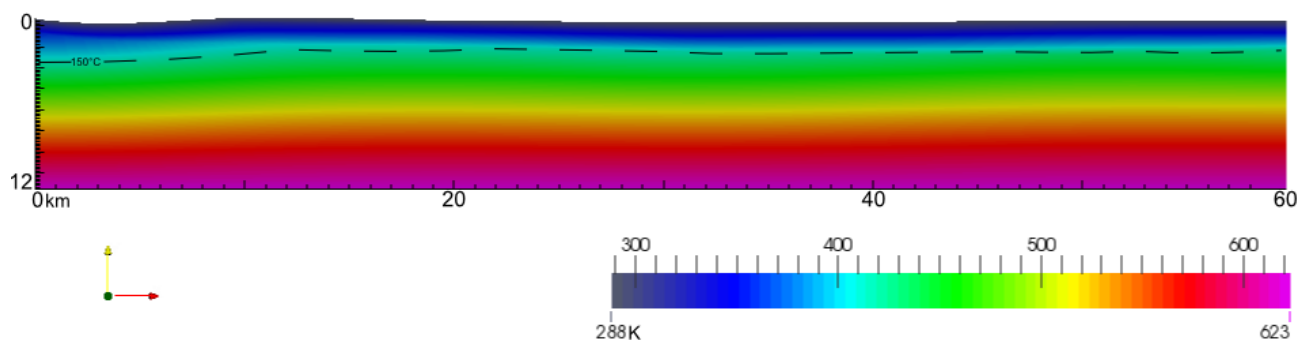


**Figure 4.3.11 Thermal profile 11 (temperature dependent): featuring 150°C/423°K isotherm, temperature scale in degrees Kelvin**

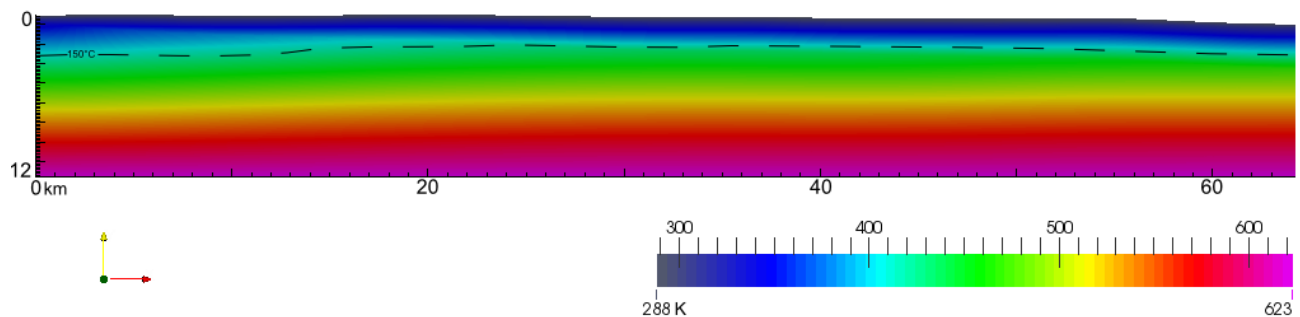


**Figure 4.3.12 Thermal profile 12 (temperature dependent): featuring 150°C/423°K isotherm, temperature scale in degrees Kelvin**

Non-temperature dependent thermal profiles are much more susceptible to temperature variation with depth than temperature dependent thermal profiles. Each geological layer is attributed a single thermal conductivity value which remains constant with temperature and therefore depth. As a result, geology and profile geometry are the main controls of temperature variation in non-temperature dependent thermal profiles. The 150°C isotherm shown in temperature dependent

thermal profiles are much more linear and instead gradually respond to geology and geometry. The temperature distribution in temperature dependent thermal profiles is by comparison smoother. Non-temperature dependent thermal profiles persistently have thermal anomalies in close proximity to the surface as demonstrated by the 150°C isotherm, most considerably in profiles 1 to 6. Thermal anomalies in profiles 1 to 6 may be due to the nature of the coal measures, where they are thickest in the north and reduce in thickness as it progresses south. The highly thermally resistive nature of the Greta coal could also significantly contribute to this in non-temperature dependent thermal profiles.

Additionally, thermal profile three interestingly shows that approximately ~35km along the profile line, the effect of topography can be seen where a local increase in sedimentary cover provides further insulation, as well as coal providing additional insulation. The top of the basement in the Western half of thermal profile three is very shallow in comparison with the Eastern half. Although as seen in profile 2, high temperatures are associated with sediment and coal thickness, but also distance to the top of the basement from heat generation through radioactive decay of heat producing elements. Although there is prominent topographic variation in profile 3, the resulting incongruence in topography, sedimentary cover, coal thickness and distance to basement ensues little disparity in temperature laterally, across the thermal profile. This profile is an example of the effect of complex geometry on the thermal structure of the Sydney Basin, and highlights the requirement for the understanding of large scale geology.

In sum, temperature dependent and non-temperature dependent thermal profiles distinctively vary from each other. Temperature field variation between temperature dependent and non-temperature thermal profiles are sufficiently significant to infer that temperature dependent thermal conductivity has an important impact in the way heat is distributed in the Sydney Basin.

## 4.4 Geotherms

In order to assess the uncertainty in our calculated downhole temperature, we utilised a Monte Carlo approach. We assigned Gaussian distributions to our temperature-dependent conductivity, based on the means and standard deviations of the temperature-dependent conductivity curves shown in Section 4.1. This method randomly sampled each distribution for each Monte Carlo simulation, for each layer for every temperature interval from 20 to 300°C. The output statistical variation is shown on geotherm plots, extracted from temperature dependent thermal profiles. A preliminary test was made with 100 iterations for profile 1. 100 iterations seem to show extremely large uncertainties at depth (greater than 6km) but show that the top 2km have very constrained geotherms with little variation. In order to determine if 100 iterations are enough to determine statistical uncertainty, we also tested 1000 iterations to considerably constrain statistical variation. A series of geotherms at 1000 iterations were plotted showing uncertainties in temperature with depth (Figure 4.4.1 to 4.4.8).

As shown in the table below, each point is a 1D geotherm with an uncertainty range at 150°C. Point 0 starts at 0km along the thermal profile and progress sequentially at 10km intervals. Beside the profile number the uncertainty range average of that profile is given. The range in uncertainty in the depth to the 150°C isotherm ranges between 99 and 389 meters across all profiles (Table 4.2). Profile points highlighted in red show minimum uncertainties within 2km from the surface and may be areas of interest regarding the potential for geothermal energy in the Sydney Basin.

Profile 1 (av. 255m)	Profile 2 (av. 389m)	Profile 3 (av. 193m)
Point 0 3156 - 3466m	Point 0 3993 - 4303m	Point 0 3063 - 3166m
Point 1 3116 - 3400m	Point 1 3838 - 4096m	Point 1 2934 - 3063m
Point 2 3027 - 3337m	Point 2 3734 - 3993m	Point 2 2779 - 2908m
Point 3 3002 - 3260m	Point 3 3476 - 3708m	Point 3 2546 - 2701m
Point 4 2924 - 3105m	Point 4 3176 - 3460m	Point 4 2494 - 2649m
Point 5 2959 - 3140m	Point 5 2882 - 3166m	Point 5 2572 - 2701m
Point 6 3063 - 3269m	Point 6 3011 - 3347m	Point 6 2391 - 2546m
Point 7 3037 - 3295m	Point 7 2779 - 3192m	Point 7 2598 - 2779m
Point 8 2804 - 3037m	Point 8 2365 - 2830m	Point 8 2804 - 3037m
Point 9 2830 - 3063m	Point 9 2184 - 2675m	Point 9 2779 - 3063m
Point 10 2779 - 3114m	Point 10 1952 - 2494m	Point 10 2882 - 3140m
Point 11 3089 - 3399m	Point 11 1926 - 2520m	Point 11 3311 - 3543m
	Point 12 1926 - 2443m	Point 12 3046 - 3305m
	Point 13 1823 - 2339m	Point 13 3192 - 3450m
		Point 14 3476 - 3708m
Profile 4 (av. 317m)	Profile 5 (av. 132m)	Profile 6 (av. 318m)
Point 0 3114 - 3250m	Point 0 3095 - 3173m	Point 0 3192 - 3605m
Point 1 2934 - 3063m	Point 1 3093 - 3190m	Point 1 2934 - 3373m
Point 2 2675 - 2779m	Point 2 3073 - 3170m	Point 2 2753 - 3179m
Point 3 2210 - 2417m	Point 3 2804 - 2934m	Point 3 2275 - 2688m
Point 4 2469 - 2727m	Point 4 2598 - 2675m	Point 4 2017 - 2417m
Point 5 2572 - 2830m	Point 5 2494 - 2649m	Point 5 1810 - 2004m
Point 6 2804 - 3373m	Point 6 2753 - 2856m	Point 6 1952 - 2159m
Point 7 3037 - 3502m	Point 7 2882 - 3089m	Point 7 1926 - 2120m
Point 8 3140 - 3683m	Point 8 2753 - 3062m	Point 8 2042 - 2210m
Point 9 2986 - 3502m	Point 9 2946 - 3063m	Point 9 2030 - 2223m
Point 10 2959 - 3269m	Point 10 2895 - 3037m	Point 10 2055 - 2456m
Point 11 2624 - 2908m	Point 11 3321 - 3411m	Point 11 2068 - 2469m
Point 12 2649 - 2934m	Point 12 3437 - 3541m	Point 12 2042 - 2456m
Point 13 3037 - 3399m	Point 13 3269 - 3386m	Point 13 2197 - 2391m
Point 14 3424 - 3889m	Point 14 2262 - 2533m	
Point 15 3295 - 3734m	Point 15 1862 - 1978m	
Point 16 3063 - 3450m	Point 16 2559 - 2624m	
Point 17 3011 - 3192m	Point 17 2804 - 2908m	
Point 18 3218 - 3347m	Point 18 2817 - 2946m	
Profile 7 (av. 271m)	Profile 8 (av. 206m)	Profile 9 (av. 99m)
Point 0 3657 - 4006m	Point 0 2456 - 2533m	Point 0 2391 - 2456m
Point 1 3192 - 3618m	Point 1 1913 - 2094m	Point 1 1849 - 1926m
Point 2 1939 - 2494m	Point 2 1926 - 2133m	Point 2 1965 - 2042m
Point 3 1448 - 1862m	Point 3 2236 - 2430m	Point 3 2210 - 2262m
Point 4 1500 - 1876m	Point 4 2391 - 2723m	Point 4 2443 - 2559m
Point 5 1732 - 2030m	Point 5 2585 - 2895m	Point 5 2572 - 2792m
Point 6 1978 - 2146m	Point 6 2662 - 2946m	Point 6 2546 - 2675m
Point 7 2107 - 2301m	Point 7 2611 - 2817m	Point 7 2417 - 2520m
Point 8 2301 - 2456m	Point 8 2533 - 2675m	Point 8 2404 - 2486m
Point 9 2314 - 2469m	Point 9 2714 - 2843m	Point 9 2598 - 2662m
Point 10 2301 - 2443m		
Point 11 2197 - 2365m		
Point 12 2120 - 2288m		
Point 13 2262 - 2430m		
Profile 10 (av. 128m)	Profile 11 (av. 233m)	Profile 12 (av. 109m)
Point 0 1913 - 2029m	Point 0 2959 - 3192m	Point 0 3024 - 3101m
Point 1 2146 - 2223m	Point 1 2249 - 2507m	Point 1 2469 - 2611m
Point 2 2004 - 2107m	Point 2 2030 - 2262m	Point 2 1875 - 2068m
Point 3 2210 - 2327m	Point 3 2094 - 2417m	Point 3 1862 - 1939m
Point 4 2378 - 2598m	Point 4 1965 - 2185m	Point 4 1978 - 2055m
Point 5 2469 - 2649m	Point 5 1849 - 1978m	Point 5 2120 - 2223m
Point 6 2430 - 2572m		Point 6 2365 - 2456m
Point 7 2482 - 2585m		
Point 8 2546 - 2637m		

**Table 4.3 Geotherm uncertainty range at 150°C and average uncertainty for each profile (points highlighted in red show minimum depth uncertainty is <2000m).**

Only a small number of geotherms can be included due to the large number of them. One geotherm per profile of geothermal interest will be shown.

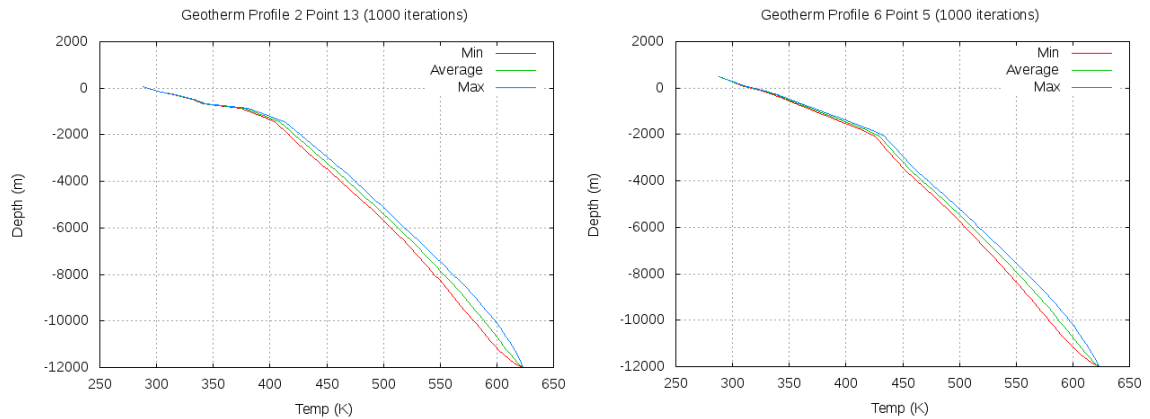


**Figure 4.4.1 Geotherm plot with s.d. of profile 2 point 13 generated at 1000 iterations. This geotherm is associated with temperature dependent thermal profile 2 (Figure 4.3.2) at 130km along the profile line. Figure 4.4.2 Geotherm plot with s.d. of profile 6 point 5 generated at 1000 iterations. This geotherm is associated with temperature dependent thermal profile 6 (Figure 4.3.6) at 50km along the profile line.**

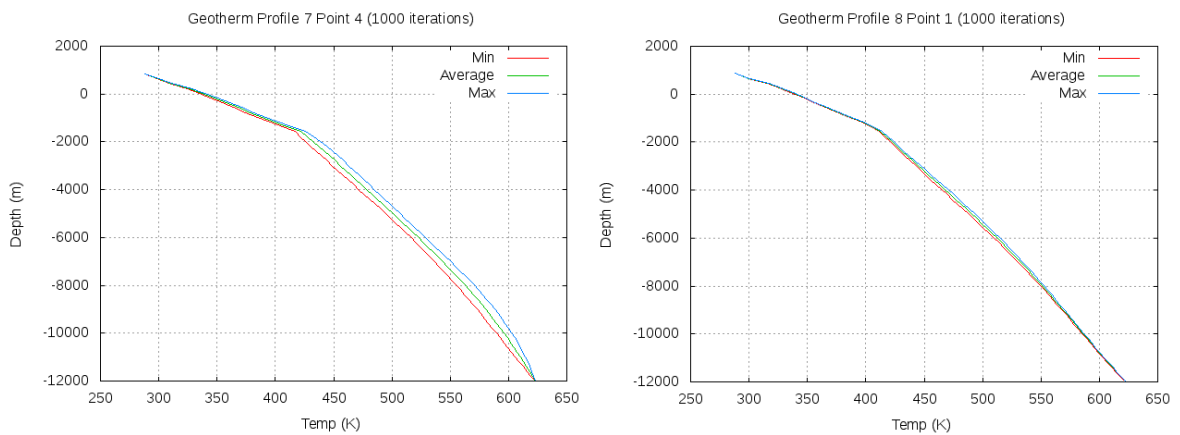


**Figure 4.4.3 Geotherm plot with s.d. of profile 7 point 4 generated at 1000 iterations. This geotherm is associated with temperature dependent thermal profile 7 (Figure 4.3.7) at 40km along the profile line. Figure 4.4.4 Geotherm plot with s.d. of profile 8 point 1 generated at 1000 iterations. This geotherm is associated with temperature dependent thermal profile 8 (Figure 4.3.8) at 10km along the profile line.**

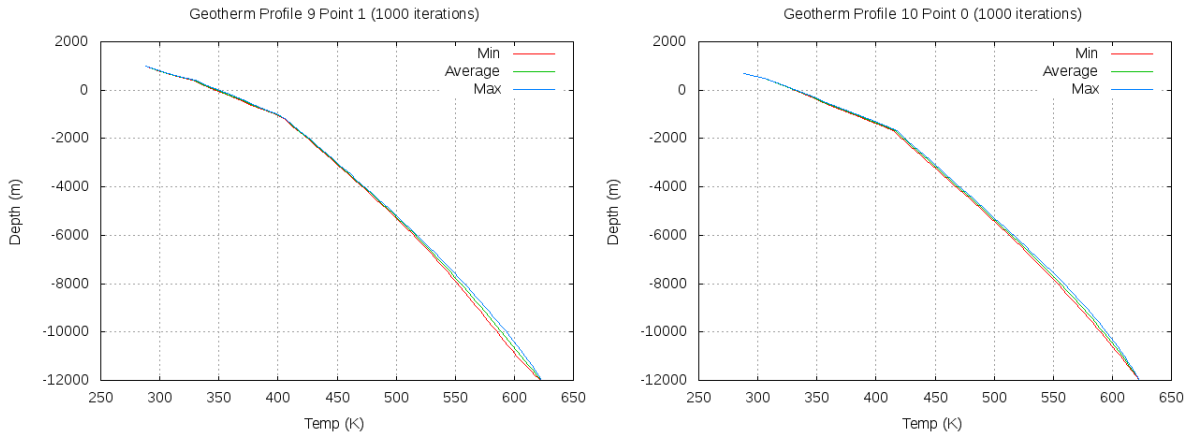


**Figure 4.4.5 Geotherm plot with s.d. of profile 9 point 1 generated at 1000 iterations. This geotherm is associated with temperature dependent thermal profile 9 (Figure 4.3.9) at 10km along the profile line. Figure 4.4.6 Geotherm plot with s.d. of profile 10 point 0 generated at 1000 iterations. This geotherm is associated with temperature dependent thermal profile 10 (Figure 4.3.10) at 0km along the profile line.**

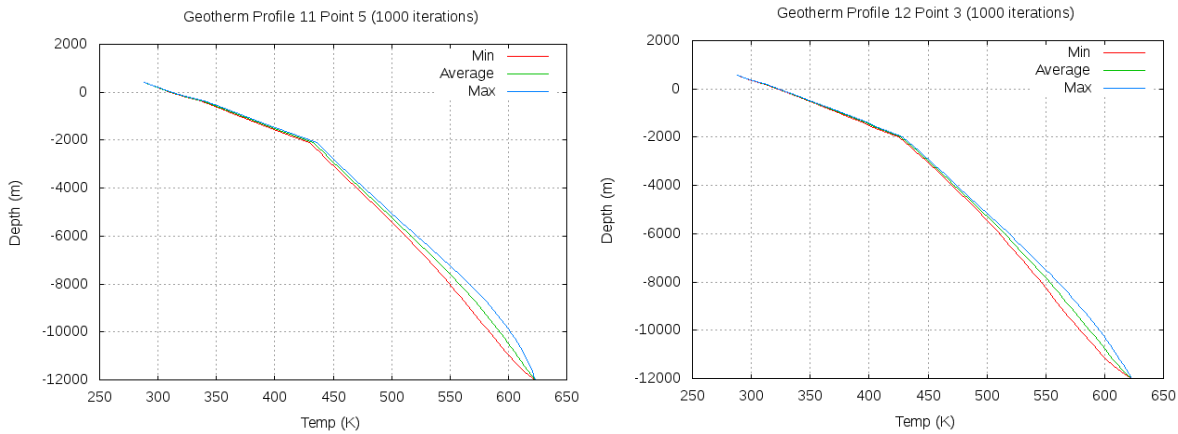


**Figure 4.4.7 Geotherm plot with s.d. of profile 11 point 5 generated at 1000 iterations. This geotherm is associated with temperature dependent thermal profile 11 (Figure 4.3.11) at 5km along the profile line. Figure 4.4.8 Geotherm plot with s.d. of profile 12 point 3 generated at 1000 iterations. This geotherm is associated with temperature dependent thermal profile 12 (Figure 4.3.12) at 30km along the profile line.**



Geotherm plots consistently display two major geothermal gradients, the first being a surface gradient and the second major geothermal gradient manifests itself at the top of the basement. Basement thermal conductivity values are not constant throughout all thermal profiles, accounting for the variation in uncertainties between geotherm plots. However, the uncertainties associated with surface layers (sediment, coal and volcanics) are largely constant.

In summary, a number of geotherm plots have indicated that certain locations may be viable for geothermal potential. 1D geotherm plots suggest a range of potential sites such as North West Singleton with critical temperatures of 150C at depths ranging from 1823 to 2339m, Wollemi National Park vicinity showing potential from 1810 to 2004m, and central area of the Blue Mountains show potential from 1448 to 1862m. The Katoomba region has potential from 1913 to 2094m, as well as South Katoomba from 1849 to 1926m, along the East coast within the Stanwell Park vicinity there is potential from 1849 to 1978m, and finally North East of Moss Vale where there may be potential from 1862 to 1939m. The site located North West of Singleton may be most appropriate for possible future testing and modelling or even perhaps reconnaissance surveys to assess its real world potential, considering proximity to existing mining infrastructure.

## 5. Discussion

### 5.1 Importance of temperature dependent thermal conductivity

Constant and temperature-dependent thermal profiles indicate that thermal conductivity has an important impact on subsurface temperature distributions. Thermal profiles using constant thermal conductivity respond very closely to basin geometry, while temperature dependent thermal profiles display a gradual change in geothermal gradient with depth.

While the effect of additional variables such as pressure and pore size is not accounted for in our thermal models, the effect of thermal conductivity in geothermal modelling seems to be of great importance (Abdulagatova et al. 2009).

Crustal thermal modelling at relatively extensive depths (eg. down to the moho discontinuity, which is approximately 35km) would especially require representative thermal conductivity values (Vosteen et al. 2003), and given the sensitivity we have seen in the range of 20-300°C, representative values may not currently exist. The crust is host to a large variety of rock types which all have very different thermal conductivities (Clauser 1995), where mineralogical and structural complexities can lead to discrete crustal structures (Goff et al. 2012).

For instance, temperature dependent thermal profile 2 exhibits a very distinct temperature distribution mainly caused by the insulating thermal properties of the Permian and Greta coal measures (Figure 4.3.2). While, constant thermal conductivity thermal profiles have irregular temperature distribution and shallower 150°C isotherms, as portrayed in Figure 4.2.2; incorporating constant thermal conductivities in thermal models has highlighted the disparity between constant and temperature dependent thermal models. Thermal anomalies associated with constant thermal conductivity thermal models could lead to misleading interpretations of the thermal structure of the Sydney Basin. Figure 5.1, demonstrates the temperature variation between constant and temperature dependent thermal profiles, beneath a thick sequence of the Greta coal measures. The constant thermal conductivity curve (in black) infers a temperature 150°C at less than 1km, whereas the temperature dependent thermal conductivity curve infers a temperature of 150°C at approximately

4km. This large offset is a strong example of the relevance of temperature dependent thermal conductivity.

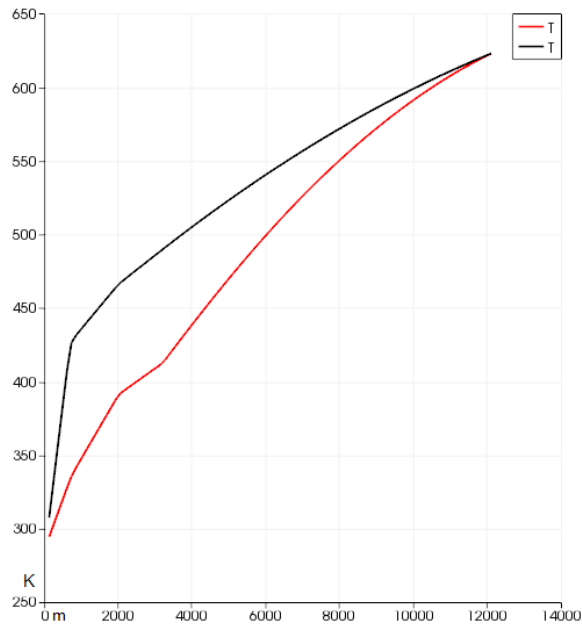


**Figure 5.1 Geothermal plot of profile 3 constant (black line) and temperature dependent (red line) thermal models (110km along the profile line).**

It is assumed in this project that pressure effects have minimal repercussions on thermal conductivity and temperature at <5km, however it is worth noting that a study led by Abdulagatova et al. (2009) measured the thermal conductivity of dry sandstone using a guarded parallel plate apparatus, which is the same type of device that our measurements were made with. Their measurements indicate that the thermal conductivity of dry sandstone linearly increases with temperature from 275 to 523°K, while also showing a linear increase with pressure from 0.1 to 400 MPa. In parallel, Petrini et al. (2000), report pressures of 30MPa at 5km depth in the crust. Interestingly, the effect of pressure as demonstrated by Abdulagatova et al. (2009) is most prominent at the lowest pressures from 0.1 to 20MPa, which would then have an effect on sedimentary rocks buried <5km from the surface, as opposed to pressures from 100 to 400MPa which show a slow and gradual increase in thermal conductivity. The variation in thermal conductivity from 0.1 to 20MPa is approximately 4%, the change is quite small and may be within error; however incorporating pressure effects in future models and investigating the role of pressure in crustal systems may well prove useful in order to further constrain the thermal structure of sedimentary basins. The thermal conductivity of Triassic sediments incorporated in

this study were however hydrated and not dried during measurements in order to somewhat stay true to natural conditions, where sedimentary rocks have generally high water content. While thermal conductivity measurements may not be directly comparable, it is worth noting that there is a large difference in values between dried and hydrated sandstone.

Drying the sandstone before measuring its thermal conductivity is perhaps not representative of the local geological conditions; however groundwater and fluid saturation are factors that should be taken into account in basin thermal modelling (Alishaev et al. 2012). Danis (2014) had previously showed that advective effects due to groundwater flow are only important in the Sydney Basin shallow Triassic sequences, such as the Hawkesbury Sandstone. Such effects are negligible in the low-permeability Permian sequences.

## **5.2 Importance of coal**

The role of coal in basin thermal structure is not well understood. Danis et al. (2012) and Danis (2014) identify that coal-bearing sedimentary basins have initially been ignored for potential geothermal resources, because of a lack of understanding of the extrapolation temperature method, to address the geological structure and the thermal properties of basin materials such as coal. Coal's insulating properties need to be included in foreland basin thermal models, because of the large quantities of coal measures that we know are there (Jones et al. 1987). The presence of thick coal measures indeed seems to have a significant impact on the thermal structure of the Sydney Basin, as shown in Danis et al. (2012), and in results presented here. Danis et al. (2012) and Rawling et al. (2014) both present models which demonstrated that coal bearing formation provide thermal insulation, which increases temperature underneath the coal measures, despite these areas exhibiting low surface heat flux. However, the unusual behaviour of coal's thermal conductivity with depth qualifies these conclusions.

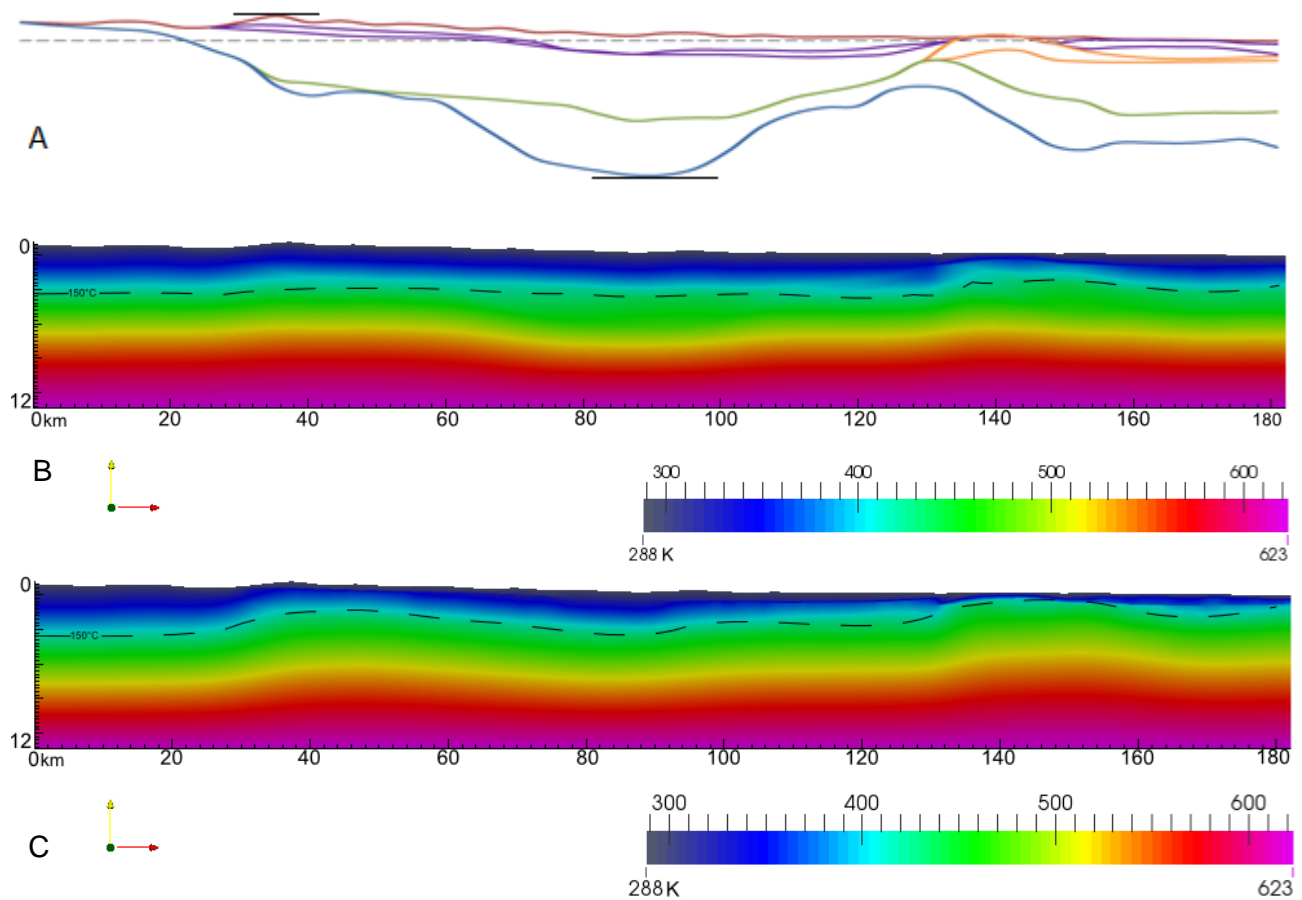


**Figure 5.2 Profile 5 extracts. Red line represents sediments, purple lines represent the Permian coal measures, orange lines represent the Greta coal measures, the green line represents the Carboniferous volcanics, and the blue line represents the top of the basement. This collage shows the effect of the thick Greta coal measures on subsurface temperatures. A) Lithological model, as described in chapter 3, top topography is 1050m and deepest point for top of basement is 5605m B) Subsurface temperatures for temperature dependent thermal conductivity within each geological unit, from table 4.1. C) Subsurface temperature for constant thermal conductivity within each geological unit, from table 4.1.**

The second, fourth and fifth thermal profiles are great example of the disparity in temperature distribution between a region of very low sedimentary cover with no coal, and a region of very thick sedimentary cover (up to 3000m) with thick Permian coal layers, and a very thick Greta coal layer which has extremely insulating thermal conductivities ( $\sim 0.3$  W/mK). Thermal profile 2 provides a direct correlation between

thick sedimentary cover and coal measures, and a shallow 150°C isotherm. The lack of sedimentary cover at the beginning of the profile (up to 80km along the profile line), results in basement heat being refracted up to this low-conductivity pathway. Thermal profile 4 exhibits two comparatively low temperature geotherms (at 80km and 145km along the profile line), which correlate with reduced coal thickness and increased distance to top of basement.

The 150°C isotherm is elevated beneath thick coal measures, as demonstrated in Figure 5.2. However, another significant effect is the thickness of the basin sediments, and the relative depth to the top of the basement. As seen in Figure 5.2, basement highs are associated with elevated 150°C.

Profile 5 has especially high geotherm temperatures beneath the coal (600m beneath surface) at 140km along the profile line, where the Greta coal measures is at its thickest (approximately ~750km thick). This thermal anomaly is directly caused by the presence of insulating coal, where the temperature profile is otherwise relatively linear.

However, in the model with temperature-dependent conductivities, the insulating effect of the coal is mitigated by its increasing conductivity for temperatures beyond 150°C. The decreasing thermal conductivity of sediments (Figure 4.1.9) over this temperature range contrasts markedly with this behaviour of coal, and the net effect is a much more subdued contrast at depth.

### **5.3 Effect of basin and basement geometry on thermal model**

The model is defined by basin and basement geometry, and the physical properties bound to the geology. Variation of basin and basement geometry in turn affect the subsurface variation in thermal conductivity itself as a function of depth and temperature. Therefore geometry, and corollary topography has a significant effect on the thermal structure of the Sydney Basin (Danis et al. 2012).

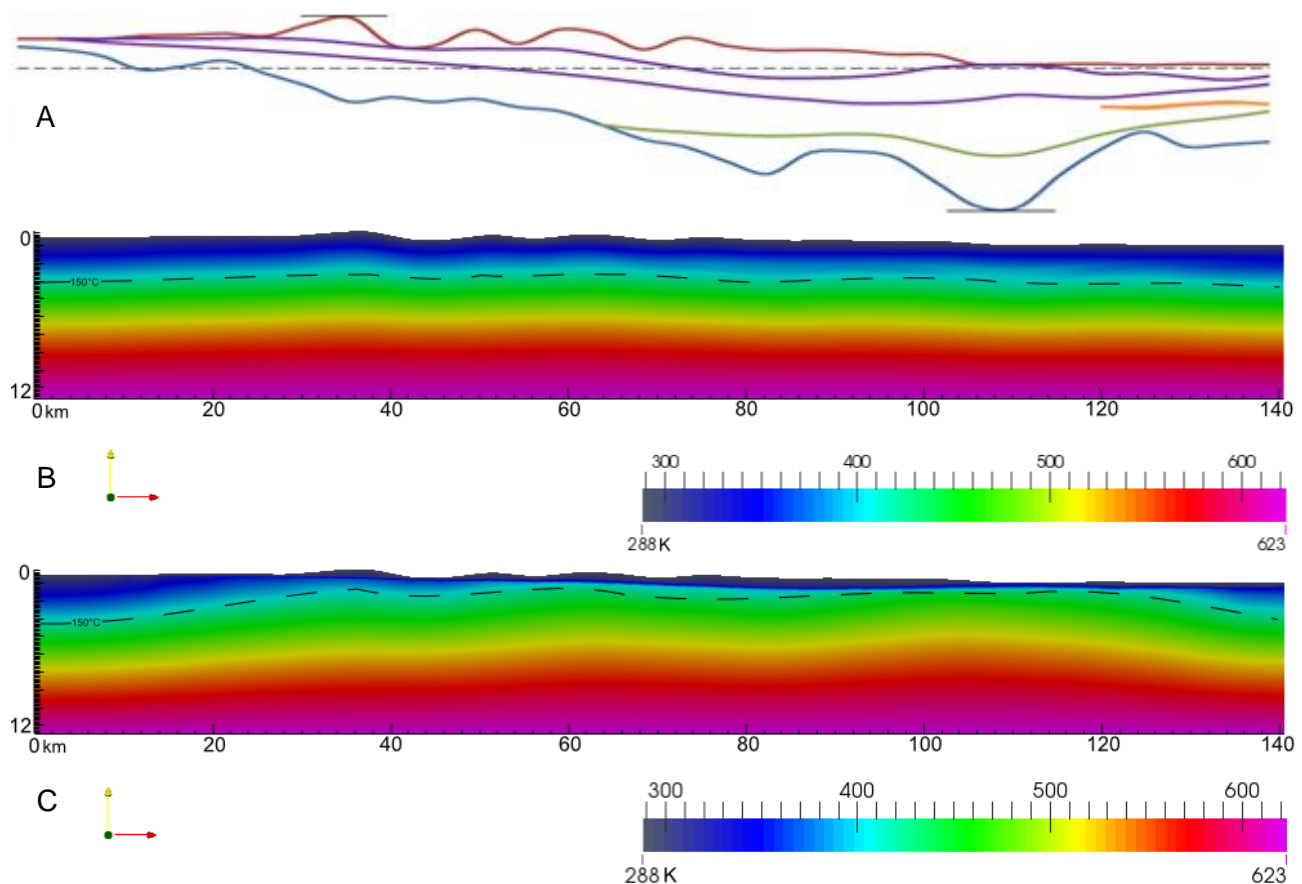


**Figure 5.3 Profile 3 extracts. Red line represents sediments, purple lines represent the Permian coal measures, orange lines represent the Greta coal measures, the green line represents the Carboniferous volcanics, and the blue line represents the top of the basement. Effect of topography and thick Permian coal measures on subsurface temperatures. A) Lithological model, as described in chapter 3, top topography is 1113m and deepest point for top of basement is 3027m B) Subsurface temperatures for temperature dependent thermal conductivity within each geological unit, from table 4.1. C) Subsurface temperature for constant thermal conductivity within each geological unit, from table 4.1.**

Thermal profile 3 addresses the importance of basin geometry through topography, where at approximately ~35km along the profile line, high topography has resulted in a local increase in sedimentary cover, together with coal providing additional insulation. The top of the basement in the Western half of thermal profile three is very shallow in comparison with the Eastern half. Again, elevated 150°C isotherms are associated with both sediment and coal thickness, and distance to the top of the basement. The latter effect is a function of both the high concentration of radiogenic

elements in the basement rocks, generating significant heat (Blevin et al. 2010), and the relatively high conductivity of crystalline basement.

Although there is prominent topographic variation in profile 3, the competing effects of topography, sedimentary cover, coal thickness and distance to basement ensures little disparity in temperature laterally, across the thermal profile. This profile is an example of the effect of complex geometry on the thermal structure of the Sydney Basin, and highlights the importance of understanding of large scale geology of a basin.

#### 5.4 Additional implications: Effect of geothermal gradient on crustal structure, rigidity and viscosity

Mechanisms for deformation within a continent are numerous and range from viscous ductile flow in the lower crust, to brittle deformation in the upper crust. The net rheology of a continent can be rather intricate Regenauer-Lieb et al. (2006) Turcotte et al. (2014).

Ideally, the viscous flow mechanism associated with mantle to crustal material is highly temperature-dependent. The seismicity and degree of brittle failure in the crust is also dependent on crustal temperatures, and high temperature isotherms affect the ductility of material in the shallow crust. As a result, the rigidity of the crust is very sensitive to the temperature at depth and geotherms Regenauer-Lieb et al. (2006).

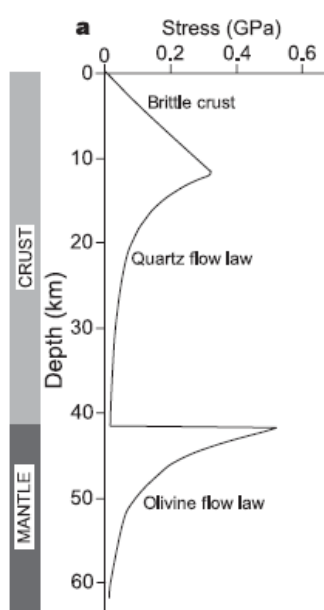




***Figure 5.4 Strength profile of the lithosphere (Simplified Brace-Goetze strength profile) extracted from Regenauer-Lieb et al. (2006).***

Figure 5.4 illustrates the stress factor of different stages of the Earth's crust and upper mantle. As a generalisation, the crust is assumed to be largely brittle, but as temperature dependent thermal models have shown, some areas such as east of thermal profile 2 have shallow 150°C isotherms lingering beneath thick Permian coal measures, and increasingly thermally resistive sediment with depth. Thermal anomalies detected in the shallow crust could also be a response to mantle convection patterns, where crustal heat essentially emanates from. This could have implications on the viscosity on the upper mantle and possible understanding of local convection cells directly below temperature anomalies detected in the shallow crust.

## 6. Conclusion

The initial aims of this study have been to compile and incorporate the basin geometry and temperature dependent thermal conductivity measurements and constant thermal conductivity values in thermal models of the Sydney Basin, and assess their relevance in terms of their effect on thermal structure.

It was found, that temperature dependent thermal models have much more restrained isotherms than non-temperature dependent thermal models. This is primarily thought to be due to the presence of coal measures, insulating heat generating basement, as well as the reduction in thermal conductivity of the sediments with temperature. Basement architecture and proximity to surface also impacts the results, where the lack of sediment in some cases leads to thermal refraction patterns found in profile 7.

Geotherm plots were used to show the uncertainty range of thermal gradients in order to confidently estimate temperatures at depth. However, the main findings of this research consist of the highly temperature dependent nature of thermal models and the impact of thermal conductivity variation on the thermal structure of the Sydney Basin.

Geotherm plots indicate the apparent viability for geothermal potential in the Sydney Basin. 1D geotherm plots suggesting the appearance of 150°C isotherms at relatively shallow depths, which are ideal as exploration targets. The range of potential sites include the North West Singleton, Wollemi National Park, Central Blue Mountains, South Katoomba and Stanwell Park vicinity, showing potential at 2km or less. North West of Singleton is thought to be the most appropriate site for possible geothermal exploration, localised thermal models would help to further constrain geothermal potential.

New understanding of the Sydney Basin thermal structure could lead to new research targets regarding geothermal potential of the Sydney Basin. The Sydney Basin may be used as a proxy for the understanding of other sites that share similar

geology. This could also perhaps prompt future interest in investing in geothermal energy both in Australia and elsewhere.

## References

- Abdulagatova, Z., Abdulagatov, I. M., & Emirov, V. N. (2009). Effect of temperature and pressure on the thermal conductivity of sandstone. *International. Journal of Rock Mechanics and Mining Sciences*, 46(6), 1055-1071.
- Alishaev, M. G., Abdulagatov, I. M., & Abdulagatova, Z. Z. (2012). Effective thermal conductivity of fluid-saturated rocks: experiment and modeling. *Engineering Geology*, 135, 24-39.
- Bangerth, W., Hartmann, R., Kanschat, G. (2007). Deal.II – a general purpose object orientated finite element library. *ACM Transactions on Mathematical Software (TOMS)*, 33(4), 1-24.
- Blevin, P.; Chappell, B.; and Jeon, H. (2010). Heat generating potential of igneous rocks within and underlying the Sydney Basin: some preliminary observations. *Proceedings of the 37th Symposium of the geology of the Sydney Basin*.
- Casareo, F. (1996). Geochemical and petrographic studies of coals in the upper Permian Whittingham coal measures, Northern Sydney Basin, NSW, Australia. North Ryde: Macquarie University.
- Clauser, C., & Huenges, E. (1995). Thermal conductivity of rocks and minerals. *Rock physics & phase relations: A handbook of physical constants*, 105-126.
- Conaghan, P. J., Jones, J. G., McDonnell, K. L., & Royce, K. (1982). A dynamic fluvial model for the Sydney Basin. *Journal of the Geological Society of Australia*, 29(1-2), 55-70.
- Conaghan, P., Jones, G., & McDonnell, K. (1987). Coal measures of an orogenic recess: Late Permian Sydney Basin, Australia. *Paleogeography, Paleoclimatology, Paleoecology*, 58(3-4), 203-219.
- Danis, C., & O'Neill, C. (2010). A static method for collecting temperatures in deep groundwater bores for geothermal exploration and other applications. *Proceedings of Groundwater*.
- Danis, C., O'Neill, C., Lackie, M., Twigg, L., Danis, A. (2011). Deep 3D structure of the Sydney Basin using gravity modelling, *Australian Journal of Earth Sciences: An International Geoscience Journal of the Geological Society of Australia*, 58(5), 517-542.
- Danis, C., O'Neill, C. Lee, J. (2012). Geothermal state of the Sydney Basin: assessment of constraints and techniques, *Australian Journal of Earth Sciences: An International Geoscience Journal of the Geological Society of Australia*, 59(1), 75-90.

Danis, C. (2014). Use of groundwater temperature data in geothermal exploration: the example of Sydney Basin, Australia. *Hydrogeology Journal*, 22(1), 87-106.

Evans, M. (2013). Thermal conductivity database of Paleozoic intrusives of Basement to the Sydney Basin. Department of Earth and Planetary Sciences, Macquarie University.

Facer, R. A.; Cook, A. C.; and Beck, A. E. (1980). Thermal properties and coal rank in rocks and coal seams of the Southern Sydney Basin, NSW: a palaeogeothermal explanation of coalification. *International Journal of Coal Geology*, 1(1), 1-17.

Finlayson, D. M. & H. M. McCracken, H. M. (1981) Crustal structure under the Sydney Basin and Lachlan Fold Belt, determined from explosion seismic studies, *Journal of the Geological Society of Australia: An International Geoscience Journal of the Geological Society of Australia*, 28(1-2), 177-190.

Gerner EJ, Holgate FL (2010) OzTemp Interpreted temperature at 5 km depth image. Available via Geoscience Australia. [http:// www.ga.gov.au/energy/geothermal-energy-resources.html](http://www.ga.gov.au/energy/geothermal-energy-resources.html),. Accessed 4 May 2011

Goff, J. A., & Holliger, K. (Eds.). (2012). Heterogeneity in the crust and upper mantle: nature, scaling, and seismic properties. Springer Science & Business Media.

Gulson, B. L., Diessel, C. F. K., Mason, D. R., & Krogh, T. E. (1990). High precision radiometric ages from the northern Sydney Basin and their implication for the Permian time interval and sedimentation rates. *Australian Journal of Earth Sciences*, 37(4), 459-469.

Greenhalgh, S. A.; Suprajitno, M.; & King, D. W. (1986). Shallow seismic reflection investigation of coal in the Sydney Basin. *Geophysics*, 51(7), 1426-1437.

Heller, P. L., Angevine, C. L., Winslow, N. S., & Paola, C. (1988). Two-phase stratigraphic model of foreland-basin sequences. *Geology*, 16(6), 501-504.

Herbert, C. (1995) Sequence stratigraphy of the Late Permian Coal Measures in the Sydney Basin, *Australian Journal of Earth Sciences: An International Geoscience Journal of the Geological Society of Australia*, 42(4), 391-405.

Hunt, J., Anderson, A., Benett, A., Brakel, A., & Whithouse, J. (1984). Petrography and geochemistry of the coals and depositional environments of the sediments in the late Permian Tomago and Newcastle coal measures from the bore Strevens Terrigal 1 - Northern Eastern Sydney Basin, NSW. North Ryde: CSIRO - Institute of Energy and Earth Resources.

Jones, J. G., Conaghan, P. J., & McDonnell, K. L. (1987). Coal measures of an orogenic recess: late Permian Sydney Basin, Australia. *Palaeogeography, palaeoclimatology, palaeoecology*, 58(3), 203-219.

Petrini, K., & Podladchikov, Y. (2000). Lithospheric pressure-depth relationship in compressive regions of thickened crust. *Journal of Metamorphic Geology*, 18(1), 67-78.

Jaupart, C., & Mareschal, J. C. (2005). Production from Heat Flow Data. *The Crust*, 3, 65.

Quenette, S., Moresi, L., O'Neill, C., & Danis, C. (2012). The effects of temperature dependent thermal conductivity on basin heat flow. *Thirty-Seventh Workshop on Geothermal Reservoir Engineering*.

Qureshi, I. R. (1989) Positive gravity anomaly over the Sydney Basin. *Exploration Geophysics*, 20(1-2), 191-193.

Rawling, T.J., Sandiford, M., Beardsmore, G.R., Quenette, S., Goyen, S.H. and Harrison, B.: Thermal insulation and geothermal targeting, with specific reference to coal-bearing basins, *Australian Journal of Earth Sciences*, 60, (2014), 817–829.

Regenauer-Lieb, K., Weinberg, R. F., & Rosenbaum, G. (2006). The effect of energy feedbacks on continental strength. *Nature*, 442(7098), 67-70.

Rezaei, H. R., Gupta, R. P., Bryant, G. W., Hart, J. T., Liu, G. S., Bailey, C. W., ... & Endo, Y. (2000). Thermal conductivity of coal ash and slags and models used. *Fuel*, 79(13), 1697-1710.

Turcotte, D. L., & Schubert, G. (2014). *Geodynamics*. Cambridge University Press.

Vila, M.; Fernandez, M.; Jimenez-Munt, I. (2010). Radiogenic heat production variability of some common lithological groups and its significance to lithospheric thermal modelling. *Technophysics*, 490(5), 152-164.

Vosteen, H. D., & Schellschmidt, R. (2003). Influence of temperature on thermal conductivity, thermal capacity and thermal diffusivity for different types of rock. *Physics and Chemistry of the Earth, Parts A/B/C*, 28(9), 499-509.

# Appendix

## The thermal model code:

```
#include <deal.II/grid/tria.h>
#include <deal.II/dofs/dof_handler.h>
#include <deal.II/grid/grid_generator.h>
#include <deal.II/grid/grid_tools.h>
#include <deal.II/grid/grid_refinement.h>
#include <deal.II/numerics/error_estimator.h>

#include <deal.II/grid/tria_accessor.h>
#include <deal.II/grid/tria_iterator.h>
#include <deal.II/dofs/dof_accessor.h>

#include <deal.II/fe/fe_q.h>

#include <deal.II/dofs/dof_tools.h>

#include <deal.II/fe/fe_values.h>
#include <deal.II/base/quadrature_lib.h>

#include <deal.II/base/function.h>
#include <deal.II/numerics/vector_tools.h>
#include <deal.II/numerics/matrix_tools.h>

#include <deal.II/lac/vector.h>
#include <deal.II/lac/full_matrix.h>
#include <deal.II/lac/sparse_matrix.h>
#include <deal.II/lac/compressed_sparsity_pattern.h>
#include <deal.II/lac/solver_cg.h>
#include <deal.II/lac/precondition.h>

#include <deal.II/numerics/data_out.h>
#include <deal.II/numerics/data_postprocessor.h>
#include <fstream>
#include <iostream>

#include <model_data.h>
#include <data_interpolation.h>
#include <thermal.h>

using namespace dealii;
model_data model;

Thermal::Thermal (const std::string &dir)
:
  fe (1),
  dof_handler (triangulation),
  //model("data",3),
  dir(dir)
/*,
  bottom(-8.0e3),
  x_start(0.e3),
  x_end(140.e3),
  top_temp(300.),
  bottom_temp(500.)*//
{
  read_config(dir);
  model.bottom = this->bottom;
  model.read_data(dir,n_layers,n_coals);
  std::cout<<"Main class initialized."<<std::endl;
```

```

}

void Thermal::read_config(const std::string &dir)
{
    std::string filename = dir;
    filename += "/config.dat";
    FILE *fp=fopen(filename.c_str(),"r");
    if(fp==NULL)
    {
        printf("Can't open file %s to read!\n",filename.c_str());
        exit(1);
    }
    else
        printf("Reading config file %s ...\n",filename.c_str());
    char *temp;
    size_t temp_i;
    temp=(char *)malloc(sizeof(char)*256);
    getline(&temp,&temp_i,fp);
    fscanf(fp,"%lf\n",&bottom);
    getline(&temp,&temp_i,fp);
    fscanf(fp,"%lf\n",&x_start);
    getline(&temp,&temp_i,fp);
    fscanf(fp,"%lf\n",&x_end);
    // Automatically make this grid close to square
    n_y=1;
    n_x=(unsigned)((x_start-x_end)/bottom);
    getline(&temp,&temp_i,fp);
    fscanf(fp,"%u\n",&n_refine);

    getline(&temp,&temp_i,fp);
    fscanf(fp,"%lf\n",&top_temp);
    getline(&temp,&temp_i,fp);
    fscanf(fp,"%lf\n",&bottom_temp);
    getline(&temp,&temp_i,fp);
    fscanf(fp,"%d\n",&n_layers);
    getline(&temp,&temp_i,fp);
    fscanf(fp,"%d\n",&n_coals);
    getline(&temp,&temp_i,fp);
    // Loop to get all the x coords for output profiles
    while(!feof(fp))
    {
        double profile_x;
        if(fscanf(fp,"%lf",&profile_x)!=1)
            break;
        x_profiles.push_back(profile_x);
    }

    fclose(fp);
    //Show setting summary
    {
        printf("Model depth          %8.1f km\n", bottom/1.e3);
        printf("Model x range          [%8.1f,%8.1f] km.\n", x_start/1.e3,
x_end/1.e3);
        printf("Cell size at [x,y]      [%8.1f,%8.1f] m.\n", (x_end-
x_start)/(n_x*pow(2,n_refine)), (0.-
bottom)/(n_y*pow(2,n_refine)));
        printf("Top/Bottom temperature [%8.1f,%8.1f] K\n", top_temp,
bottom_temp);
        printf("Number of layers        %d\n", n_layers);
        printf("Number of coal layers   %d\n", n_coals);
        printf("Number of profiles      %lu\n", x_profiles.size());
    }
}

```



```

Point<2> grid_transform (const Point<2> &in)
{
    Point<2> out;

    out(0) = in(0);
    out(1) = in(1) + model.get_topo(in(0)) * (1.0-in(1)/model.bottom);
    //printf("[%8.2e,%8.2e]->[%8.2e,%8.2e]\n",in(0),in(1),out(0),out(1));
    return out;
}

void Thermal::refine_grid ()
{
    Vector<float> estimated_error_per_cell (triangulation.n_active_cells());
    KellyErrorEstimator<2>::estimate (dof_handler,
                                      QGauss<1>(3),
                                      typename FunctionMap<2>::type(),
                                      solution,
                                      estimated_error_per_cell);
    GridRefinement::refine_and_coarsen_fixed_number (triangulation,
                                                    estimated_error_per_cell,
                                                    0.3, 0.03);
    triangulation.execute_coarsening_and_refinement ();
}

void Thermal::make_grid ()
{
    //GridGenerator::hyper_cube (triangulation, -1, 1);
    //Triangulation<2>::cell_iterator cell=triangulation.begin();
    //cell->face(0)->set_boundary_indicator(1);
    //cell->face(1)->set_boundary_indicator(2);
    Point<2> p1(x_start,0);
    Point<2> p2(x_end,bottom);
    std::vector< unsigned int > repetitions(2);
    repetitions[0]=n_x;
    repetitions[1]=n_y;

    GridGenerator::subdivided_hyper_rectangle(triangulation,repetitions,p1,p2,true)
    ;

    triangulation.refine_global (n_refine);
    GridTools::transform(grid_transform, triangulation);
    /*
    std::cout << "Number of active cells: "
                << triangulation.n_active_cells()
                << std::endl;

    std::cout << "Total number of cells: "
                << triangulation.n_cells()
                << std::endl;
    */
    std::cout << "Grid is made."<<std::endl;
}

void Thermal::setup_system_0 ()
{
    dof_handler.distribute_dofs (fe);
    std::cout << "Number of degrees of freedom: "
                << dof_handler.n_dofs()
                << std::endl;

    CompressedSparsityPattern c_sparsity(dof_handler.n_dofs());
    DoFTools::make_sparsity_pattern (dof_handler, c_sparsity);

```

```

sparsity_pattern.copy_from(c_sparsity);

system_matrix.reinit (sparsity_pattern);

solution.reinit (dof_handler.n_dofs(),true);
for(unsigned i=0;i<dof_handler.n_dofs();i++)
    solution[i]=400.;
solution_dT.reinit (dof_handler.n_dofs());
system_rhs.reinit (dof_handler.n_dofs());
}

void Thermal::setup_system ()
{
    system_matrix.reinit (sparsity_pattern);
    solution_dT.reinit (dof_handler.n_dofs());
    system_rhs.reinit (dof_handler.n_dofs());
}

void Thermal::assemble_system_0 ()
{
    QGauss<2> quadrature_formula(2);
    FEValues<2> fe_values (fe, quadrature_formula,
                          update_values | update_gradients | update_JxW_values
                          | update_quadrature_points);
    const unsigned int dofs_per_cell = fe.dofs_per_cell;
    const unsigned int n_q_points = quadrature_formula.size();

    FullMatrix<double> cell_matrix (dofs_per_cell, dofs_per_cell);
    Vector<double> cell_rhs (dofs_per_cell);

    std::vector<types::global_dof_index> local_dof_indices (dofs_per_cell);

    DoFHandler<2>::active_cell_iterator
    cell = dof_handler.begin_active(),
    endc = dof_handler.end();
    for (; cell!=endc; ++cell)
    {
        fe_values.reinit (cell);

        cell_matrix = 0;
        cell_rhs = 0;

        std::vector<double> T(n_q_points);
        fe_values.get_function_values(solution, T);

        for (unsigned int i=0; i<dofs_per_cell; ++i)
            for (unsigned int j=0; j<dofs_per_cell; ++j)
                for (unsigned int q_point=0; q_point<n_q_points; ++q_point)
                {
                    Point<2> Q=fe_values.quadrature_point(q_point);
                    //double K=get_K(Q,400.);
                    double K=model.get_K(Q[0],Q[1],T[q_point]);
                    cell_matrix(i,j) += (fe_values.shape_grad (i, q_point) *
                                         fe_values.shape_grad (j, q_point) *
                                         fe_values.JxW (q_point))* K;
                }

        for (unsigned int i=0; i<dofs_per_cell; ++i)
            for (unsigned int q_point=0; q_point<n_q_points; ++q_point)
            {
                Point<2> Q=fe_values.quadrature_point(q_point);
                cell_rhs(i) += (fe_values.shape_value (i, q_point) *
                               model.get_H(Q[0],Q[1]) * // H *
                               fe_values.JxW (q_point));
            }
    }
}

```

```

        cell->get_dof_indices (local_dof_indices);

        for (unsigned int i=0; i<dofs_per_cell; ++i)
            for (unsigned int j=0; j<dofs_per_cell; ++j)
                system_matrix.add (local_dof_indices[i],
                                   local_dof_indices[j],
                                   cell_matrix(i,j));
        for (unsigned int i=0; i<dofs_per_cell; ++i)
            system_rhs(local_dof_indices[i]) += cell_rhs(i);
    }

    std::map<types::global_dof_index,double> boundary_values;

    VectorTools::interpolate_boundary_values (dof_handler,
                                              2,
                                              ConstantFunction<2>(bottom_temp),
                                              boundary_values);
    VectorTools::interpolate_boundary_values (dof_handler,
                                              3,
                                              ConstantFunction<2>(top_temp),
                                              boundary_values);

    MatrixTools::apply_boundary_values (boundary_values,
                                        system_matrix,
                                        solution,
                                        system_rhs);
}

void Thermal::assemble_system ()
{
    QGauss<2> quadrature_formula(2);
    FEValues<2> fe_values (fe, quadrature_formula,
                          update_values | update_gradients | update_JxW_values
                          | update_quadrature_points);
    const unsigned int dofs_per_cell = fe.dofs_per_cell;
    const unsigned int n_q_points = quadrature_formula.size();

    FullMatrix<double> cell_matrix (dofs_per_cell, dofs_per_cell);
    Vector<double> cell_rhs (dofs_per_cell);

    std::vector<types::global_dof_index> local_dof_indices (dofs_per_cell);

    DoFHandler<2>::active_cell_iterator
    cell = dof_handler.begin_active(),
    endc = dof_handler.end();
    for (; cell!=endc; ++cell)
    {
        fe_values.reinit (cell);

        cell_matrix = 0;
        cell_rhs = 0;
        cell->get_dof_indices (local_dof_indices);
        std::vector<Tensor<1, 2>> solution_gradients(n_q_points);
        std::vector<double> T(n_q_points);
        fe_values.get_function_gradients(solution, solution_gradients);
        fe_values.get_function_values(solution, T);

        for (unsigned int i=0; i<dofs_per_cell; ++i)
            for (unsigned int j=0; j<dofs_per_cell; ++j)
                for (unsigned int q_point=0; q_point<n_q_points; ++q_point)
                {
                    Point<2> Q=fe_values.quadrature_point(q_point);
                    //double K=get_K(Q,T[q_point]);
                }
    }
}

```

```

        //double dK_dT=get_dK_dT(Q,T[q_point]);
        double K=model.get_K(Q[0],Q[1],T[q_point]);
        double dK_dT=model.get_dK_dT(Q[0],Q[1],T[q_point]);
        cell_matrix(i,j) += (fe_values.shape_grad (i, q_point) *
                             fe_values.shape_grad (j, q_point) *
                             fe_values.JxW (q_point)) * K
                             + (fe_values.shape_grad (i, q_point) *
                                solution_gradients [q_point] *
                                fe_values.shape_value (j, q_point) *
                                fe_values.JxW (q_point)) * dK_dT ;
        cell_rhs(i) += - (fe_values.shape_grad (i, q_point) *
                          solution_gradients [q_point] *
                          fe_values.JxW (q_point)) * K
                          + (fe_values.shape_value (i, q_point) *
                             fe_values.JxW (q_point)) * model.get_H(Q[0],Q[1])
// Can replace 0.0 with heat production rate
        ;
    }

    for (unsigned int i=0; i<dofs_per_cell; ++i)
        for (unsigned int j=0; j<dofs_per_cell; ++j)
            system_matrix.add (local_dof_indices[i],
                              local_dof_indices[j],
                              cell_matrix(i,j));

    for (unsigned int i=0; i<dofs_per_cell; ++i)
        system_rhs(local_dof_indices[i]) += cell_rhs(i);
}
std::map<types::global_dof_index,double> boundary_values;

for(unsigned i=2;i<4;i++)
    VectorTools::interpolate_boundary_values (dof_handler,
                                              i,
                                              ConstantFunction<2>(0.),
                                              boundary_values);

MatrixTools::apply_boundary_values (boundary_values,
                                    system_matrix,
                                    solution_dT,
                                    system_rhs);
}

void Thermal::solve_0 ()
{
    SolverControl          solver_control (3000, 1e-12);
    SolverCG<>             solver (solver_control);

    solver.solve (system_matrix, solution, system_rhs,
                 PreconditionIdentity());
}

void Thermal::solve ()
{
    SolverControl          solver_control (3000, 1e-12);
    SolverCG<>             solver (solver_control);

    solver.solve (system_matrix, solution_dT, system_rhs,
                 PreconditionIdentity());
}

template <int dim>

```

```

class Thermal::Postprocessor : public DataPostprocessor<dim>
{
public:
    Postprocessor(const class Thermal *this_parent):
        this_parent(this_parent)
    {
    };
    virtual
    void
    compute_derived_quantities_scalar (const std::vector<double> >
&uh,
                                     const std::vector<Tensor<1,dim> >
&duh,
                                     const std::vector<Tensor<2,dim> >
&dduh,
                                     const std::vector<Point<dim> >
&normals,
                                     const std::vector<Point<dim> >
&evaluation_points,
                                     std::vector<Vector<double> >
&computed_quantities) const
    {
        const unsigned int n_quadrature_points = uh.size();
        Assert (computed_quantities.size() == n_quadrature_points,
ExcInternalError());
        for(unsigned int q=0;q<n_quadrature_points;++q)
        {
            computed_quantities[q](0) = uh[q];
            //computed_quantities[q](1) = this_parent-
>get_K(evaluation_points[q],uh[q]);
            //computed_quantities[q](2) = this_parent-
>get_dK_dT(evaluation_points[q],uh[q]);
            computed_quantities[q](1) = /*this_parent-
>*/model.get_K(evaluation_points[q][0],evaluation_points[q][1],uh[q]);
            computed_quantities[q](2) = /*this_parent-
>*/model.get_dK_dT(evaluation_points[q][0],evaluation_points[q][1],uh[q]);
            computed_quantities[q](3) = /*this_parent-
>*/model.get_H(evaluation_points[q][0],evaluation_points[q][1]);
            computed_quantities[q](4) = /*this_parent-
>*/model.get_material(evaluation_points[q][0],evaluation_points[q][1]);
        }
    };

    virtual std::vector<std::string> get_names () const
    {
        std::vector<std::string> solution_names(1,"T");
        solution_names.push_back ("K");
        solution_names.push_back ("dK_dT");
        solution_names.push_back ("H");
        solution_names.push_back ("Material_ID");
        return solution_names;
    };
    virtual unsigned int n_output_variables() const
    {
        return 5;
    };

    virtual
    std::vector<DataComponentInterpretation::DataComponentInterpretation>
    get_data_component_interpretation () const
    {
        std::vector<DataComponentInterpretation::DataComponentInterpretation>
            interpretation
(1,DataComponentInterpretation::component_is_scalar);

```

```

interpretation.push_back(DataComponentInterpretation::component_is_scalar);
interpretation.push_back(DataComponentInterpretation::component_is_scalar);
interpretation.push_back(DataComponentInterpretation::component_is_scalar);
interpretation.push_back(DataComponentInterpretation::component_is_scalar);
    return interpretation;
};

    virtual UpdateFlags get_needed_update_flags () const
    {
        return update_values | update_q_points;
    };
private:
    const class Thermal *this_parent;
};

void Thermal::output_results (const std::string &dir) const
{
    DataOut<2> data_out;
    data_out.attach_dof_handler (dof_handler);
    //data_out.add_data_vector (solution,"T");
    Postprocessor<2> postprocessor(this);
    data_out.add_data_vector (solution, postprocessor);
    data_out.add_data_vector (solution_dT,"dT");
    data_out.build_patches ();

    std::string filename = dir+ "/output";
    //if(cycle==0)system(("mkdir "+filename).c_str());
    filename += "/solution";
    filename += ".vtk";
    std::ofstream output (filename.c_str());
    data_out.write_vtk (output);
    // Output thermal profiles

    for(unsigned i=0;i<x_profiles.size();i++)
    {
        char profile_name[256];
        sprintf(profile_name,"%s/output/profile.%u",dir.c_str(),i);
        printf("Outputing profile %u...\n",i);
        output_profile(std::string(profile_name),x_profiles[i]);
    }
}

void Thermal::output_profile(const std::string &filename, double x) const
{
    //printf("Start outputing profile\n");
    //const std::vector<Point<2> > support_points
    // = fe.get_unit_support_points();
    Quadrature<2> support_points(fe.get_unit_support_points());
    std::vector<bool> point_mark(dof_handler.n_dofs(),false);
    std::vector<struct Data_point> data_points;
    FEValues<2> fe_values (fe,support_points,
                          update_values |
                          update_quadrature_points |
                          update_JxW_values);
    //printf("Before the loop\n");
    const unsigned int dofs_per_cell = fe.dofs_per_cell;
    std::vector<types::global_dof_index> local_dof_indices (dofs_per_cell);
    typename DoFHandler<2>::active_cell_iterator cell =
dof_handler.begin_active(),
                                endc = dof_handler.end();

```

```

const double critial_dist = 0.5*(x_end-x_start)/(n_x*pow(2,n_refine));
for (; cell!=endc; ++cell)
{
    fe_values.reinit(cell);
    //printf("Loop over cell\n");
    const std::vector<Point<2> > vertex_points
        = fe_values.get_quadrature_points();
    //printf("%d points\n",vertex_points.size());
    //printf("Trying to get temperature from %d temperature
solutions\n",solution.size());
    std::vector<double> cell_temperature(dofs_per_cell);
    fe_values.get_function_values(solution, cell_temperature);
    //printf("%d cell temperatures get.\n",cell_temperature.size());
    cell->get_dof_indices (local_dof_indices);
    for(unsigned i=0;i<dofs_per_cell;i++)
    {
        //printf("Loop over dofs of the cell\n");
        //printf("Checking point %8d [%8.1f,%8.1f] distant/critical
[%8.1f,%8.1f].\n",
        //      local_dof_indices[i], vertex_points[i][0], vertex_points[i][1],
        //      fabs(vertex_points[i][0]-x), critial_dist);
        if(fabs(vertex_points[i][0]-x)<=critial_dist)
        {
            if(point_mark[local_dof_indices[i]]==false)
            {
                //Add point into array
                //printf("Add a point\n");
                struct Data_point data_point;
                data_point.id      = local_dof_indices[i];
                data_point.point    = vertex_points[i];
                data_point.temperature = solution[local_dof_indices[i]];

                data_points.push_back(data_point);
                point_mark[local_dof_indices[i]]=true;
            }
        }
    }
    printf("%8lu points found in this profile (%8d vertial grid
points).\n",data_points.size(),n_y*(int)pow(2,n_refine)+1);
    //Sort array
    std::sort(data_points.begin(),data_points.end());

    //Save into file
    FILE *fp=fopen(filename.c_str(),"w");
    if(fp!=NULL)
    {
        //Write the header
        fprintf(fp,"%18s %18s %18s %18s\n","Y","T","X","ID");
        for(unsigned i=0;i<data_points.size();i++)
        {
            fprintf(fp,"%18e %18e %18e %18lu\n", data_points[i].point[1]
                , data_points[i].temperature
                , data_points[i].point[0]
                , data_points[i].id);
        }
        printf("Temperature profile wrote into %s\n",filename.c_str());
        fclose(fp);
    }
    else
    {
        printf("Can't open file %s to write temperature
profile.\n",filename.c_str());
    }
}

```

```

double Thermal::compute_residual (const double alpha) const
{
    Vector<double> residual (dof_handler.n_dofs());
    Vector<double> evaluation_point (dof_handler.n_dofs());
    evaluation_point = solution;
    evaluation_point.add (alpha, solution_dT);
    const QGauss<2> quadrature_formula(2);
    FEValues<2> fe_values (fe, quadrature_formula,
                          update_values      |
                          update_gradients   |
                          update_quadrature_points |
                          update_JxW_values);

    const unsigned int      dofs_per_cell = fe.dofs_per_cell;
    const unsigned int      n_q_points    = quadrature_formula.size();
    Vector<double>          cell_residual (dofs_per_cell);
    std::vector<Tensor<1, 2>> gradients(n_q_points);
    std::vector<double> T(n_q_points);
    std::vector<types::global_dof_index> local_dof_indices (dofs_per_cell);
    residual = 0;
    typename DoFHandler<2>::active_cell_iterator cell =
dof_handler.begin_active(),
                                                    endc = dof_handler.end();

    for (; cell!=endc; ++cell)
    {
        cell_residual = 0;
        fe_values.reinit (cell);
        fe_values.get_function_gradients (evaluation_point,
                                          gradients);
        fe_values.get_function_values(evaluation_point, T);
        for (unsigned int q_point=0; q_point<n_q_points; ++q_point)
        {
            Point<2> Q=fe_values.quadrature_point(q_point);
            //double K=get_K(Q,T[q_point]);
            double K=model.get_K(Q[0],Q[1],T[q_point]);
            for (unsigned int i = 0; i < dofs_per_cell; ++i)
                cell_residual(i) +=
                    (fe_values.shape_grad(i, q_point)
                     * gradients[q_point]
                     * K
                     * fe_values.JxW(q_point)
                     - fe_values.shape_value(i, q_point)
                     * model.get_H(Q[0],Q[1]) //H
                     * fe_values.JxW(q_point));
        }
        cell->get_dof_indices (local_dof_indices);
        for (unsigned int i=0; i<dofs_per_cell; ++i)
            residual(local_dof_indices[i]) += cell_residual(i);
    }
    //hanging_node_constraints.condense (residual);
    std::vector<bool> boundary_dofs (dof_handler.n_dofs());
    DoFTools::extract_boundary_dofs (dof_handler,
                                     ComponentMask(),
                                     boundary_dofs);
    for (unsigned int i=0; i<dof_handler.n_dofs(); ++i)
        if (boundary_dofs[i] == true)
            residual(i) = 0;
    return residual.l2_norm();
}

double Thermal::compute_residual () const
{
    double residual=0.,volume=0.;
    const QGauss<2> quadrature_formula(3);
    FEValues<2> fe_values (fe, quadrature_formula,
                          update_values      |

```



```

                                update_quadrature_points |
                                update_JxW_values);
const unsigned int             dofs_per_cell = fe.dofs_per_cell;
const unsigned int             n_q_points   = quadrature_formula.size();
std::vector<Tensor<1, 2>> > gradients(n_q_points);
std::vector<double> dT(n_q_points);
std::vector<types::global_dof_index> local_dof_indices (dofs_per_cell);
typename DoFHandler<2>::active_cell_iterator cell =
dof_handler.begin_active(),
                                endc = dof_handler.end();

for (; cell!=endc; ++cell)
{
    fe_values.reinit (cell);
    fe_values.get_function_values(solution_dT, dT);
    for (unsigned int q_point=0; q_point<n_q_points; ++q_point)
    {
        residual += fabs(dT[q_point] * fe_values.JxW(q_point)) ;
        volume    += fe_values.JxW(q_point);
    }
}
//hanging_node_constraints.condense (residual);
return residual / volume;
}

void Thermal::run ()
{
    double relaxation_factor = 0.3;
    int n_iterations = 15;
    for (unsigned int cycle=0; cycle<n_iterations; ++cycle)
    {
        std::cout << "Cycle " << cycle << ':' << std::endl;
        if (cycle == 0)
        {
            make_grid ();
        }
        //else
        //refine_grid ();

        std::cout << " Number of active cells: "
                    << triangulation.n_active_cells()
                    << std::endl;
        if (cycle ==0) setup_system_0();
        std::cout << " Number of degrees of freedom: "
                    << dof_handler.n_dofs()
                    << std::endl;
        if(cycle==0)
        {
            //output_results (dir,cycle);
            std::string filename = dir+ "/output";
            system(("mkdir "+filename).c_str());
            assemble_system_0 ();
            solve_0 ();
            output_results (dir);
        }
        setup_system ();
        assemble_system ();
        solve ();
        /*
        std::cout << "Average temperature change for Non-linear steps: "
                    << compute_residual()
                    << std::endl;
        */
        double nonlinear_residual = compute_residual(relaxation_factor);
        std::cout << "Non-linear residual: "
                    << nonlinear_residual

```

```

        << std::endl;
    solution.add(relaxation_factor,solution_dT);
    if(nonlinear_residual<1.e-5)
    {
        printf("Converged in %d steps.\n",cycle);
        break;
    }

}
output_results (dir);
//Varify solutions
/*
{
    Vector<double> old_solution = solution;
    setup_system ();
    assemble_system_0 ();
    solve_0 ();
    for(unsigned i=0;i<solution.size();i++)
        solution_dT[i] = solution[i] - old_solution[i];
    std::cout << "Average temperature change when varifying the solution: "
        << compute_residual()
        << std::endl;
}*/
//output_results (dir,n_iterations);
}

int main (int argc, char *argv[])
{
    std::string dir;
    if (argc >= 2)
        dir = argv[1];
    else
    {
        printf("Usage: Thermal data_directory.\n");
        exit(1);
    }
    //model.read_data(dir);
    Thermal thermal_problem(dir);
    std::cout<<"Starting main programe."<<std::endl;
    thermal_problem.run ();

    return 0;
}

```

